https://doi.org/10.5194/egusphere-2026-3149
Preprint. Discussion started: 25 June 2026

Impacts of mesh refinement on the simulation of a long-range transported extreme dust storm over East Asia in the global variable-resolution model (iAMAS v2.6.3)

Yibo Xue[1], Chun Zhao[1,2,3,4,5], Jiawang Feng[1], Xin Qu[1], Zihan Xia[1], Zining Yang[1], Xiaoxiao Zhang[6], Qike Yang[1], Gudongze Li[1], Ziyu Zhang[1], Jianxi Zhang[1]

[1]*School of Earth and Space Sciences, University of Science and Technology of China, Hefei, China*
[2]*Joint Laboratory of Fengyun Remote Sensing, University of Science and Technology of China, Hefei, China*
[3]*State Key Laboratory of Fire Science, University of Science and Technology of China, Hefei, China*
[4]*Institute of Advanced Interdisciplinary Research on High-Performance Computing Systems and Software, University of Science and Technology of China, Hefei, China*
[5]*Laoshan Laboratory, Qingdao, China*
[6]*State Key Laboratory of Ecological Safety and Sustainable Development in Arid Lands, Xinjiang Institute of Ecology and Geography, Chinese Academy of Sciences, Urumqi, China*

Correspondence: Chun Zhao (chunzhao@ustc.edu.cn)

https://doi.org/10.5194/egusphere-2026-3149
Preprint. Discussion started: 25 June 2026

Abstract: Long-range transported dust storms challenge regional high-resolution models because lateral boundary conditions constrain the consistent representation of dust emission, transport, and deposition. Here we use the integrated Atmospheric Model Across Scales (iAMAS v2.6.3), a global variable-resolution physics-chemistry coupled model, to simulate the extreme East Asian dust storm from 13 to 18 March 2021. Three experiments adopt a globally quasi-uniform 50 km mesh (U50 km) and two source-refined meshes at 16-50 km (V16 km) and 4-50 km (V4 km). Evaluated against reanalysis and ground-based observations, the simulations reproduce the large-scale synoptic evolution, while mesh refinement captures more detailed near-surface dynamical features and terrain-channeled winds through improved topographic representation. The model reasonably represents 10-m wind speed, surface PM_{10} concentrations, and aerosol optical depth. Relative to U50 km, total dust emissions over East Asia increase by 35.24% in V16 km and 54.98% in V4 km, as refined meshes resolve localized friction-velocity enhancement and nonlinear saltation-threshold exceedances. By altering emission evolution and its interaction with atmospheric circulation, mesh refinement also affects the spatial distribution of transported dust. The contrast between V16 km and V4 km reveals regional heterogeneity in downwind dust mass loading, with V4 km capturing localized wet-scavenging enhancement not evident in V16 km and reducing dust loading over the Yangtze River Delta by 30.49% relative to U50 km. This research emphasizes the importance of mesh refinement for representing long-range transported dust storms and provides a basis for future evaluations of multiple dust emission schemes in global variable-resolution models.

https://doi.org/10.5194/egusphere-2026-3149
Preprint. Discussion started: 25 June 2026

1. Introduction

Dust aerosols have significant impacts on the atmospheric environment and human health by altering the Earth's radiation balance, affecting cloud microphysical processes, and inducing respiratory diseases (Woodage et al., 2010; Chen et al., 2013; IPCC, 2023; Tobías et al., 2025). East Asia is one of the most active dust source regions globally, frequently experiencing severe dust storms that originate from the arid and semi-arid zones of northwest China and Mongolia. Driven by strong westerly circulation, these dust plumes can be transported over long distances and affect densely populated downwind areas (Idrissa et al., 2024). Dense dust aerosols substantially increase concentrations of inhalable particles, leading to reduced visibility and severe air quality deterioration (Xue et al., 2025). Moreover, dust deposition into the North Pacific supplies bioavailable nutrients that can enhance oceanic primary productivity (Jickells et al., 2005). Given the high socio-economic vulnerability of East Asia to dust storm disasters, improving the accuracy of dust forecasting remains an urgent scientific priority.

Numerical simulations have become an indispensable tool for elucidating the mechanisms, evolution, and climatic and environmental impacts of extreme dust events. Despite substantial improvements in dust models over recent decades, accurately predicting extreme dust processes remains challenging due to the inherent nonlinearity and multi-scale interactions in dust emission and transport. Previous studies have used global models to simulate dust emissions, transport, and spatiotemporal variations, including those over East Asia, and to assess their climatic and radiative implications (Grini et al., 2005; Sun et al., 2012; Kok et al., 2017; Wu et al., 2019). However, significant uncertainty remains in simulating extreme dust events. A main limitation is that many global models still use relatively coarse horizontal meshes. Enhancing model resolution has been shown to markedly improve simulations of severe dust events, as it enables a clearer depiction of land–atmosphere coupling and surface heterogeneity (Adebiyi et al., 2020; Feng et al., 2023; Chappell et al., 2024). Global high-resolution simulations can more accurately capture dust

https://doi.org/10.5194/egusphere-2026-3149
Preprint. Discussion started: 25 June 2026

emission and long-range transport (Gu et al., 2022; Idrissa et al., 2024), yet the high computational costs limit their widespread application. In contrast, regional models with relatively high spatial resolution have been widely employed to simulate dust emission, transport, and deposition and their subsequent environmental effects (Konaré et al., 2008; Marsham et al., 2011). However, regional models depend strongly on lateral boundary conditions provided by global models (Pérez et al., 2006; Feng et al., 2023). This dependence often leads to numerical inconsistencies, including discontinuities in meteorological fields, imbalances between dynamical and thermodynamic variables, and weakened feedback of regional processes to the large-scale atmospheric circulation.

The development of global variable-resolution atmospheric models provides more opportunities for improving simulations of extreme dust events. Compared with traditional regional models, these frameworks can reduce uncertainties associated with lateral boundary conditions, better capture interactions between regional processes and large-scale circulation, and achieve regional refinement at substantially lower computational cost than globally uniform high-resolution simulations (Rauscher et al., 2013; Zarzycki & Jablonowski, 2014; Huang et al., 2016; Gu et al., 2022; Feng et al., 2023). In recent years, global variable-resolution models have been increasingly applied to study multi-scale atmospheric processes, including extreme precipitation, regional circulation, and aerosol or dust transport (Rauscher et al., 2013; Huang et al., 2016; Feng et al., 2023, 2025; Xu et al., 2023, 2024; Gu et al., 2025; Li et al., 2024, 2025). Rauscher et al. (2013) showed that regional mesh refinement in a multiresolution framework can improve simulations of regional climate patterns, while Huang et al. (2016) further demonstrated the capability of higher-resolution configurations in representing regional circulation and precipitation variability. Recent applications have also shown that variable-resolution frameworks can improve simulations of extreme rainfall events by better representing multi-scale interactions between regional processes and large-scale circulation (Xu et al., 2023, 2024; Gu et al., 2025). Li et al. (2024, 2025) further applied such frameworks to moisture

https://doi.org/10.5194/egusphere-2026-3149
Preprint. Discussion started: 25 June 2026

transport over the Tibetan Plateau and Indian summer monsoon rainfall, demonstrating their capability in representing regional water-vapor transport and monsoon-related precipitation processes. For dust-related applications, Feng et al. (2023, 2025) extended global variable-resolution modeling frameworks to dust simulations and dust-monsoon interactions, highlighting their potential for studying dust aerosols and their climatic impacts.

For extreme dust storms, kilometer-scale refinement is particularly important because dust emission and transport are strongly influenced by near-surface winds, land-surface heterogeneity, topography, and mesoscale circulation. However, relatively few studies have evaluated global variable-resolution models with kilometer-scale regional refinement for an individual extreme dust storm event. Feng et al. (2023) developed a global variable-resolution dust modeling framework with a sectionalized aerosol representation, which improved the simulation of dust particle size distribution and dust mass loading compared with traditional modal schemes. Nevertheless, the performance of this framework in reproducing the evolution of an individual severe dust storm, as well as its sensitivity to regional mesh refinement, has not been systematically assessed. In this study, we employed the integrated Atmospheric Model Across Scales (iAMAS, v2.6.3), a global variable-resolution atmospheric physics-chemistry coupled modeling framework, to simulate an intense East Asian dust storm and evaluate its ability to reproduce the event evolution. The sensitivity of model performance to mesh refinement is further investigated. The selected case is the severe dust storm that occurred over East Asia from 13 to 18 March 2021, recognized as one of the strongest dust episodes in recent years. Using iAMAS, we compared a globally quasi-uniform mesh with two regionally refined high-resolution configurations. The main objective of this study is to examine whether high-resolution regional mesh refinement within a global variable-resolution framework can improve the representation of extreme dust processes relative to a globally quasi-uniform coarse-resolution configuration, and to clarify the underlying physical mechanisms. The simulations are evaluated using reanalysis data and

https://doi.org/10.5194/egusphere-2026-3149
Preprint. Discussion started: 25 June 2026

ground-based observations.

This article is structured as follows. Section 2.1 briefly introduces the iAMAS modeling framework. Sections 2.2–2.3 describe the parameterization schemes adopted in the dust modeling framework, followed by the experimental design and model configurations in Section 2.4 and the observational datasets used for model evaluation in Section 2.5. Section 3.1 presents the model evaluation results, while Section 3.2 investigates the effects of mesh refinement on dust storm simulations. Finally, Section 4 provides the main conclusions.

2. Methodology

2.1. iAMAS

The iAMAS is a global variable-resolution atmospheric physics-chemistry coupled modeling system developed on the Sunway heterogeneous high-performance computing architecture (Gu et al., 2022; Feng et al., 2023). It adopts the dynamical core of the Model for Prediction Across Scales–Atmosphere (MPAS-A; Skamarock et al., 2012) and employs a spherical centroidal Voronoi tessellation (SCVT) mesh with C-grid staggering (Thuburn et al., 2009; Ringler et al., 2010; Skamarock et al., 2012). The SCVT mesh discretizes the sphere into unstructured polygonal cells (predominantly hexagons), thereby avoiding the polar singularities inherent to latitude-longitude grids and enabling smoothly varying horizontal resolution (Ringler et al., 2008, 2010). By prescribing a spatially varying density function during mesh generation, iAMAS supports seamless regional refinement within a single global mesh without the need for nested domains (Ju et al., 2011; Ringler et al., 2010). As a global modeling system, iAMAS enables simulations across a wide range of spatial scales, from planetary circulation to convection-permitting resolutions, within a unified dynamical framework. This multiscale capability is advantageous for dust modeling because key processes controlling dust emission and long-range transport, including terrain-modulated winds, boundary-layer mixing, and mesoscale frontal dynamics, are highly sensitive to model resolution and the spatial scales represented

https://doi.org/10.5194/egusphere-2026-3149
Preprint. Discussion started: 25 June 2026

in the simulation (Heinold et al., 2013; Chappell et al., 2024). In addition, the variable-resolution global mesh allows refined simulations over major dust source regions while retaining a globally consistent representation of downwind transport and dust-related impacts.

2.2. Dust emission scheme

Feng et al. (2023) coupled a GOCART-based dust scheme into the iAMAS framework. Here, we implemented the Shao physically based dust scheme to better represent emission processes during severe dust storm events. The Shao-type schemes explicitly consider key wind-erosion processes, including saltation bombardment and aggregate disintegration, and thus provide a physically based description of the nonlinear dependence of dust emission on near-surface wind stress and soil properties (Shao, 2001, 2004; Shao et al., 2011; hereafter S01, S04, and S11, respectively). Previous studies have shown that Shao-type schemes improve dust storm simulations by better linking dust emission with wind forcing and soil conditions (Kang et al., 2011; Wu et al., 2016; Idrissa et al., 2024). We adopted the S04 formulation. Compared with S01, S04 simplifies the emission formulation while retaining physically based representations of saltation bombardment and aggregate disintegration. Unlike the more simplified S11 scheme, S04 preserves a more explicit representation of these key emission mechanisms for size-resolved dust emission simulations (Shao, 2001, 2004; Shao et al., 2011). **Fig. 1** shows the dust source function used in the model and the major regions analyzed in this study. The main dust sources include the Taklimakan Desert (TKD), the Mongolian Gobi Desert (MGD), the Hexi Corridor-Western Inner Mongolia (HC-WIM), and the Loess Plateau (LP), while the North China Plain (NCP) and the Yangtze River Delta (YRD) are major downwind regions.

Within the S04 framework, the vertical emission flux depends on surface friction velocity and streamwise saltation mass flux, reflecting the role of saltation bombardment in transferring kinetic energy to the soil surface and initiating dust release. Dust is released primarily through saltation bombardment and, under stronger

https://doi.org/10.5194/egusphere-2026-3149
Preprint. Discussion started: 25 June 2026

erosion conditions, through the disintegration of soil aggregates, which shifts the emitted size distribution from the minimally disturbed to the fully disturbed soil particle-size spectrum (Shao et al., 1993; Alfaro and Gomes, 2001; Shao, 2004). Emission occurs only after saltation is initiated. Once the wind stress exceeds the threshold required for saltation, the horizontal saltation flux increases rapidly and provides a sustained source of energy for continued dust release from the surface (Shao and Lu, 2000).

Following S04, two limiting soil particle-size distributions are defined for a given soil: the minimally disturbed distribution $p_m(d)$ and the fully disturbed distribution $p_f(d)$. The aggregate-bound component is then defined as $p_c(d) = p_f(d) - p_m(d)$, representing the fraction of dust stored in aggregates that can be released only through mechanical destruction. Based on these distributions, the total dust fraction releasable from a unit soil mass and the aggregate-bound dust fraction are computed by integrating over the dust size range $[0, d_d]$:

$$\eta_f = \int_0^{d_d} p_f(d)\mathrm{d}d \tag{1}$$

$$\eta_c = \eta_f - \eta_m = \int_0^{d_d} p_c(d)\mathrm{d}d \tag{2}$$

where η_m denotes the free-dust fraction (i.e., dust not bound in aggregates).

For practical calculations in a sectional framework, the dust size range is discretized into *I* size bins, each characterized by a representative diameter d_i and a bin width Δd_i. The free-dust fraction in bin i is evaluated by integrating $p_m(d)$ across the bin bounds:

$$\eta_{mi} = \int_{d-\Delta d_i/2}^{d+\Delta d_i/2} p_m(d)\mathrm{d}d \tag{3}$$

The corresponding total dust fraction in bin i is partitioned as:

$$\eta_{fi} = \eta_{mi} + \eta_{ci} \tag{4}$$

where η_{ci} is the aggregate-bound dust fraction in bin i.

Given these bin-resolved soil fractions, the spectral vertical dust emission flux for dust bin *i* generated by saltation of grains with diameter d_s is expressed as:

https://doi.org/10.5194/egusphere-2026-3149
Preprint. Discussion started: 25 June 2026

$$F(d_i, d_s) = c_y \eta_{fi}\left[(1-\gamma) + \gamma \sigma_p\right](1+\sigma_m)\frac{gQ(d_s)}{u_*^2} \quad (5)$$

where c_y is a dimensionless coefficient, g is the gravitational acceleration, $Q(d_s)$ is the streamwise saltation mass flux associated with saltators of size d_s, and u_* is the surface friction velocity. The transition factor γ is specified as:

$$\gamma = exp[-(u_* - u_{*t})^3] \quad (6)$$

where u_{*t} is the threshold friction velocity for the initiation of saltation. Because Q is obtained from a saltation (sand-drift) formulation and is effectively nonzero only once saltation begins, the combined dependence on Q and $u_* - u_{*t}$ ensures that the scheme is activated only under conditions where saltation is possible (Owen, 1964; Shao, 2004).

The parameter σ_m is the ratio between the mass ejected by bombardment and the mass of the impacting particle, and can be interpreted as the bombardment efficiency:

$$\sigma_m = \frac{m_\Omega}{m} \quad (7)$$

The ratio σ_p, representing the free-dust contribution relative to the fully disturbed dust content in bin *i*, is defined as:

$$\sigma_p = \frac{\eta_{mi}}{\eta_{fi}} = \frac{p_m(d_i)}{p_f(d_i)} \quad (8)$$

Separating the contributions of free dust and aggregate-related dust yields:

$$F(d_i, d_s) = c_y[\eta_{mi} + (1-\gamma)\eta_{ci}](1+\sigma_m)\frac{gQ(d_s)}{u_*^2} \quad (9)$$

This form highlights that, under weak erosion conditions (large γ), emission is dominated by free dust (η_{mi}), whereas under strong erosion (small γ) the aggregate-bound component (η_{ci}) becomes increasingly important through the $(1-\gamma)\eta_{ci}$ term. If $\eta_{mi} \ll \eta_{fi}$, the expression can be further simplified to:

$$F(d_i, d_s) = c_y\eta_{fi}(1-\gamma)(1+\sigma_m)\frac{gQ(d_s)}{u_*^2} \quad (10)$$

which emphasizes the role of aggregate disintegration when free dust is scarce.

For practical implementation, S04 adopts the expression for σ_m derived from

https://doi.org/10.5194/egusphere-2026-3149
Preprint. Discussion started: 25 June 2026

the impact-removal formulation of Lu and Shao (1999):

$$\sigma_m = 12u_*^2 \frac{\rho_b}{p}\left(1 + 14u_*\sqrt{\frac{\rho_b}{p}}\right) \quad (11)$$

where ρ_b is soil bulk density and p is soil plastic pressure. This dependence implies that, for the same wind forcing, smaller p (looser and weaker soils) yields larger σ_m and more efficient dust production, whereas larger p (harder or crusted soils) suppresses bombardment-driven release.

The emission rate for dust bin i is obtained by integrating over the saltating particle-size range:

$$F(d_i) = \int_{d_1}^{d_2} F(d_i, d_s)\, p(d_s)\mathrm{d}d_s \quad (12)$$

where d_1 and d_2 define the lower and upper size limits of saltating particles, and $p(d_s)$ denotes the saltator size distribution used for weighting. In this study, Q is computed using a saltation scheme following Owen (1964). The total dust emission over the target dust interval is then computed by summing over all dust bins.

2.3. Dust size parameterization

In this study, mineral dust is represented using a sectional (size-bin) formulation, in which the grid-box total emission is redistributed into a finite set of diameter intervals to account for size-dependent transport, deposition, and radiative effects (Zhao et al., 2010, 2011, 2013; Feng et al., 2023). Within each bin, particles are assumed to share identical prescribed physical properties, and sub-bin variability is not explicitly represented. Following common practice in global dust modeling, the emitted particle-number size spectrum is described in log-diameter space by a log-normal distribution:

$$\frac{dN}{d(\ln d)} = \frac{N_{total}}{\sqrt{2\pi}\ln\sigma_n} exp\left[-\frac{(\ln d - \ln d_n)^2}{2(\ln\sigma_n)^2}\right] \quad (13)$$

where d is particle diameter, N_{total} is the total number concentration, d_n is the number-median diameter, and σ_n is the geometric standard deviation. Because the sectional module partitions emitted dust by volume (and equivalently by mass under fixed particle density) rather than by number, the number distribution is mapped to a

https://doi.org/10.5194/egusphere-2026-3149
Preprint. Discussion started: 25 June 2026

volume distribution using the spherical-particle relationship $V_P = \frac{\pi d^3}{6}$. This transformation preserves the log-normal form in $\ln d$, yielding a volume spectrum centered at a volume-median diameter d_v related to d_n by:

$$ln\, d_v = ln\, d_n + 3(ln\, \sigma_n)^2 \quad (14)$$

To represent the fact that emitted dust often exhibits a broader spectrum than a single log-normal mode, many schemes approximate the emitted spectrum using a two-mode log-normal mixture with fixed weights assigned to fine and coarse modes (Zhao et al., 2013). Here, bulk emissions are redistributed using prescribed bin-wise emitted volume fractions (**Table 1**) following Feng et al. (2023), ensuring a consistent emitted size partition for the sectional dust module. Although **Table 1** reports the full 10-bin partition spanning approximately 0.039-40 μm, only bins 1-8 are explicitly represented in this study because super-coarse particles (>10 μm) undergo rapid gravitational settling and near-source deposition, contributing little to long-range transport and to the evaluation metrics considered here (Feng et al., 2023). Accordingly, dust emission in this study refers to the emission integrated over the represented size range (≤10 μm).

For the *i*-th size bin with lower and upper diameter bounds D_L and D_U, the emitted volume fraction can be obtained by analytically integrating the log-normal volume distribution over the bin interval:

$$v_{bin} = \frac{1}{2} erf\left(\frac{ln\, D_U - ln\, d_v}{\sqrt{2}\, ln\, \sigma_n}\right) - \frac{1}{2} erf\left(\frac{ln\, D_L - ln\, d_v}{\sqrt{2}\, ln\, \sigma_n}\right) \quad (15)$$

where v_{bin} denotes the dust volume fraction assigned to a given size bin, and $erf(\cdot)$ is the Gaussian error function that arises from integrating a normal distribution. The bin boundaries and emitted volume fractions follow the prescribed configuration summarized in **Table 1**. For each bin, particles are treated as uniformly distributed and are represented by the geometric-mean diameter ($D_G = \sqrt{D_L D_U}$) under the spherical-particle assumption.

2.4. Numerical experiments

To evaluate the influence of horizontal resolution on dust emission and transport

https://doi.org/10.5194/egusphere-2026-3149
Preprint. Discussion started: 25 June 2026

processes, three mesh configurations are designed: a globally quasi-uniform 50 km resolution mesh (U50 km) and two global variable-resolution meshes refined to 16–50 km (V16 km) and 4–50 km (V4 km). In both variable-resolution simulations, the refinement region is centered near northwestern Gansu Province, China (41°N, 91°E) to cover the major dust source regions in East Asia and the main downwind transport pathways **(Fig. 2)**. Meteorological initial conditions and surface boundary fields are obtained from the ERA5 reanalysis at 6-hourly intervals and interpolated onto the iAMAS mesh. All experiments cover 8–20 March 2021, with 00:00 UTC 8 March to 00:00 UTC 12 March treated as a spin-up period to accumulate dust mass and allow the dynamical, thermodynamic, and chemical fields to adjust. Following the restart strategy used in variable-resolution global simulations (Feng et al., 2023), the meteorological fields are reinitialized at 00:00 UTC 12 March to reduce potential numerical drift and maintain a physically consistent large-scale atmospheric state, whereas chemical tracers, including dust, are retained from the end of the spin-up period. All chemical species are therefore continuous across the restart, which prevents artificial discontinuities in concentration fields and preserves the physical continuity of dust emission, transport, and deposition.

To isolate the effects of horizontal resolution, all experiments use the same set of physical and chemical schemes without additional tuning. The physical schemes include the Yonsei University (YSU) planetary boundary layer scheme (Hong et al., 2006), the Noah land surface model (Chen and Dudhia, 2001), the Rapid Radiative Transfer Model for General Circulation Models (RRTMG) for longwave and shortwave radiation (Mlawer et al., 1997; Iacono et al., 2008), and the Thompson microphysics scheme (Thompson et al., 2008). The Grell–Freitas cumulus convection scheme (Grell & Freitas, 2014) is used to represent subgrid convection. Because the variable-resolution mesh includes both fine and coarse cells, the Grell–Freitas cumulus scheme is retained to parameterize unresolved convection, especially in coarse-resolution regions. The V4 km experiment therefore approaches convection-permitting scales in the refined domain. Chemical process schemes for

https://doi.org/10.5194/egusphere-2026-3149
Preprint. Discussion started: 25 June 2026

simulating dust-cycle processes, including dust transport, wet removal, and dust optical properties, are represented following Feng et al. (2023). The contributions of parameterized convective and grid-scale resolved precipitation are distinguished when analyzing precipitation changes, wet scavenging, and dust evolution.

2.5. Observation and reanalysis data

To assess the ability of iAMAS to reproduce the dust storm episode during 13–18 March 2021, large-scale meteorological conditions and near-surface and column aerosol indicators are evaluated using reanalysis products and ground-based observations. Synoptic-scale circulation is characterized using ERA5 daily mean sea-level pressure, geopotential height, and wind fields (Hersbach et al., 2020). Because direct dust measurements are sparse over East Asia, daily mean PM_{10} concentrations from the China National Environmental Monitoring Center (CNEMC) are used as an observational proxy for near-surface dust concentrations. During this strong dust storm event, PM_{10} increased substantially at many observational sites, and the elevated concentrations were dominated by mineral dust, making PM_{10} an appropriate observational constraint for dust model evaluation. Daily mean surface wind speed is obtained from NOAA station observations compiled in the Global Surface Summary of the Day (GSOD) dataset. Column-integrated aerosol loading is evaluated using AErosol RObotic NETwork (AERONET) sun-photometer observations. The AERONET Version 3 Direct-Sun Level 2.0 daily mean aerosol optical depth (AOD) product is used, and missing days are supplemented with the corresponding Level 1.5 product (Giles et al., 2019). To preferentially retain dust-dominated observations, the daily mean Ångström exponent (500–870 nm) is further required to be below 0.8, indicating enhanced coarse-mode aerosol contributions typical of mineral dust (Shin et al., 2019). Because this screening substantially reduces the number of valid AERONET records during the event, event-mean AOD at 500 nm from 13 to 18 March 2021 is used, yielding 23 sites for comparison.

https://doi.org/10.5194/egusphere-2026-3149
Preprint. Discussion started: 25 June 2026

3. Results

3.1. Evaluation of the simulations

3.1.1. Synoptic condition

To characterize the synoptic-scale forcing associated with this dust event and to establish a dynamical reference for subsequent evaluation, we compared ERA5 synoptic fields with those simulated by iAMAS using the U50 km, V16 km, and V4 km mesh configurations during 13–16 March 2021 **(Fig. 3)**. Overall, all three simulations capture the main synoptic features represented in ERA5. The position and orientation of the East Asian mid-tropospheric trough at 500 hPa are generally well reproduced. The associated trough–ridge pattern and its eastward progression are also reasonably represented. Mean sea level pressure shows similar agreement. In particular, the Siberian–Mongolian high-pressure system exhibits a comparable spatial pattern and coherent day-to-day evolution in ERA5 and in all simulations. These results indicate that the three mesh configurations share a broadly consistent large-scale circulation background, providing an appropriate context for assessing the impacts of mesh refinement.

The lower-tropospheric circulation at 850 hPa shows greater sensitivity to horizontal resolution **(Fig. 3)**. Because the experiments differ mainly in resolution within the refined region, some differences outside that region may also be related to circulation adjustments associated with refinement, possibly through terrain–flow interactions (Laprise, 2008; Rauscher et al., 2013). In ERA5 and the U50 km simulation, the 850 hPa winds are relatively smooth and exhibit weak horizontal gradients. With mesh refinement, the flow becomes more spatially structured. Local contrasts in the wind field increase, and a narrower band of stronger winds emerges along major terrain transitions. This feature is especially evident near the Hexi Corridor and along the southern and eastern margins of the Mongolian Plateau. It extends toward North China, suggesting stronger terrain modulation of the low-level flow. Relative to the V16 km mesh, the V4 km simulation further reveals finer-scale directional turning and more localized wind features. These patterns are consistent

https://doi.org/10.5194/egusphere-2026-3149
Preprint. Discussion started: 25 June 2026

with stronger terrain-induced turning and channeling that are less evident at coarser resolution. Overall, these differences suggest that mesh refinement allows a clearer depiction of lower-tropospheric dynamical structures.

The 700 hPa geopotential height and wind fields (**Fig. S1**) evolve similarly in ERA5 and the three experiments, further indicating that the broader synoptic environment is well represented. Compared with the quasi-uniform U50 km simulation, the refined configurations show slightly sharper gradients at 700 hPa, although these differences are weaker than those at 850 hPa. Such sensitivity is potentially important for dust simulations because dust emission and initial transport are tightly linked to surface stress, boundary-layer turbulence, and mesoscale flow organization (Marsham et al., 2011; Klose & Shao, 2012). Higher resolution may also improve the representation of terrain–flow interactions and the downward transfer of momentum (Zhao et al., 2016), which can affect how variability in low-level winds is translated to the surface. As a result, resolution-dependent circulation variations may contribute to differences in friction velocity, dust emission fluxes, and subsequent transport pathways (Klose & Shao, 2012; Huo et al., 2025).

3.1.2. Near-surface wind speed

Daily mean 10-m wind speed (u_{10}) provides an observational benchmark for assessing the realism of the modeled near-surface wind environment (Jiménez and Dudhia, 2012). Here we evaluated simulated daily mean u_{10} against collocated NOAA surface-station observations during 13–16 March 2021 **(Fig. 4)**. Overall, all experiments capture the spatiotemporal evolution of strong near-surface winds over the study region. Enhanced winds are concentrated over the Mongolian Plateau and Inner Mongolia, exhibiting episodic strengthening as the cold-air outbreak progresses southeastward. The timing and broad spatial distribution of strong winds in the simulations are generally consistent with the observations, indicating that the synoptic-scale forcing and its near-surface manifestation are reasonably represented. Resolution-dependent differences mainly appear in the spatial organization and intensity contrasts of the strong-wind belt. The U50 km experiment produces

https://doi.org/10.5194/egusphere-2026-3149
Preprint. Discussion started: 25 June 2026

smoother and spatially broader high-wind regions, whereas V16 km and V4 km resolve sharper transitions and more confined wind corridors along major terrain boundaries. These differences suggest a stronger expression of terrain-modulated flow features, which can affect the spatial variability of surface stress and, ultimately, the distribution of wind friction velocity (u^*) (Shao, 2001; Kok et al., 2014). It is worth noting that u_{10} is evaluated here as an observationally constrained indicator of the near-surface dynamical environment rather than as a direct driver of dust emission. Emission-relevant mechanisms are assessed explicitly using u^* in Section 3.2.2.

The station-based temporal correlation coefficients (r), derived from daily mean u_{10} time series at collocated NOAA surface stations and further averaged within each region, increase markedly with mesh refinement **(Table 2)**. In the U50 km experiment, correlations are generally low (r = 0.05-0.34), with relatively weak correlation over the HC–WIM (r = 0.05) and MGD (r = 0.15). With mesh refinement to V16 km, correlations increase markedly in every region (r = 0.56-0.87) and remain high in V4 km (r = 0.81-0.92), indicating that higher resolution better captures the day-to-day variability and spatial heterogeneity of near-surface winds. Normalized mean bias (NMB) also shows clear regional contrasts. Over the primary upwind source regions, the coarse-mesh simulation substantially underestimates near-surface winds, with large negative NMB in the MGD (NMB = –53.37%) and the HC–WIM (NMB = –61.73%). Mesh refinement evidently alleviates these low biases, reducing NMB to –14.43% (MGD) and –13.92% (HC–WIM) in V16 km and further to –11.46% and –10.17% in V4 km, respectively. In contrast, several downwind regions exhibit persistent positive biases. In the U50 km experiment, u_{10} is overestimated over the LP, NCP, and YRD, with NMB values of +26.71%, +35.52%, and +29.51%, respectively. Relative to U50 km, mesh refinement substantially reduces these positive biases. The NMB decreases to +14.93% (LP), +8.02% (NCP), and +11.53% (YRD) in V16 km, and to +12.83% (LP), +7.93% (NCP), and +9.56% (YRD) in V4 km. These improvements suggest that refined meshes better capture the regional variability and magnitude of near-surface winds, likely because higher resolution provides a clearer

https://doi.org/10.5194/egusphere-2026-3149
Preprint. Discussion started: 25 June 2026

depiction of terrain-modulated flow and associated mesoscale post-frontal wind structures (Rauscher et al., 2013). In particular, better-resolved terrain may increase form drag and enhance effective surface resistance at the regional-mean scale (Jiménez and Dudhia, 2012; Feng et al., 2023). At the same time, complex topography can still permit localized channeling and localized acceleration in terrain corridors, contributing to spatially varying wind-speed biases (Zhao et al., 2019).

3.1.3. Surface PM_{10} concentration

To evaluate iAMAS performance in simulating surface PM_{10} concentrations during this strong dust event, daily mean PM_{10} concentrations over eastern China from 14 to 18 March 2021 are compared with CNEMC measurements **(Fig. 5)**. Observations indicate pronounced long-range transport, with elevated PM_{10} concentrations extending southeastward under northerly to northwesterly flow, forming a coherent high-concentration band over the NCP, the YRD, and the Shandong Peninsula during 15–16 March. All three simulations reproduce the primary transport pathway of the dust plume, indicating that the transport pattern of this event is reasonably captured. Nevertheless, resolution sensitivity is evident in both the magnitude and spatial structure of the simulated dust plumes. In the U50 km experiment, elevated PM_{10} concentrations are more spatially diffuse with muted local maxima, and the high-concentration band appears less continuous along the main transport corridor. This suggests an overly broadened plume and elevated background concentrations despite weaker local peaks, consistent with the positive mean bias presented in **Fig. 6**. The V16 km simulation better captures the spatial distribution of high PM_{10} concentrations and maintains the band-like structure during southeastward transport, forming a more coherent dust-laden corridor over eastern China. With further mesh refinement to V4 km, both peak concentrations and fine-scale spatial variability are better captured, and the simulated high-concentration regions align more closely with the observations. These results indicate that mesh refinement influences not only the simulated PM_{10} magnitude but also the spatial organization and dispersion of transported dust plumes.

https://doi.org/10.5194/egusphere-2026-3149
Preprint. Discussion started: 25 June 2026

The scatterplot provides a quantitative assessment of these simulation differences **(Fig. 6)**. All three experiments show positive correlations with the observed PM_{10} concentrations, although their bias characteristics differ markedly. The U50 km simulation reveals a pronounced positive bias, with an NMB of +44.21%. The variable-resolution V16 km configuration increases the correlation coefficient (r = 0.65) but exhibits an even larger positive bias (NMB = +57.51%). This indicates that moderate refinement improves the spatial distribution and continuity of transported dust plumes, but may still amplify the overall positive bias. The V4 km experiment further increases the correlation coefficient (r = 0.85) and reduces the NMB to below 20%, indicating that the finest mesh provides the most balanced improvement in reproducing the observed spatial variability of surface PM_{10} concentrations and downwind transport pathways. Overall, the qualitative comparison in **Fig. 5** and the quantitative statistics in **Fig. 6** consistently demonstrate the strong sensitivity of simulated surface PM_{10} concentrations to horizontal resolution.

These resolution-dependent differences in the simulated spatial distribution of dust transport may result from the combined effects of the spatiotemporal evolution of dust emissions, circulation-related wind changes, and wet scavenging in downwind regions. Dust emitted at different times may encounter different stages of the evolving synoptic circulation and boundary-layer conditions, thereby affecting its subsequent transport direction and plume pathway. Changes in the spatial distribution of emissions can also modify where dust initially enters the transport flow, leading to different downstream concentration patterns even under broadly similar large-scale circulation. In addition, resolution-induced changes in low-level winds and wet scavenging may further influence plume dispersion, transport pathway, and removal during transport. Previous studies have shown that coarse-resolution models tend to smooth terrain undulations and surface roughness, which can weaken terrain-guided near-surface acceleration and localized strong-wind features near mountain foothills and basin edges (Kok et al., 2014; Mahowald et al., 2014). Such changes in near-surface winds may affect the occurrence, intensity, and spatial distribution of

https://doi.org/10.5194/egusphere-2026-3149
Preprint. Discussion started: 25 June 2026

friction-velocity exceedances above the emission threshold, thereby modulating where and when dust is emitted and how it enters the early-stage transport flow (Shao, 2004). Regional mesh refinement can further improve the representation of terrain-modulated winds, boundary-layer structure, and associated transport pathways, allowing the same large-scale circulation to produce different downstream plume organization and dispersion characteristics (Hu et al., 2019; Feng et al., 2023). These specific influencing mechanisms will be examined in detail in Section 3.2.

3.1.4. AOD

As a column-integrated measure of aerosol loading, AOD is widely used to characterize aerosol burden and diagnose regional transport during dust storms (Giles et al., 2019; Hu et al., 2019). Ground-based AERONET AOD at 500 nm is used as the primary observational benchmark for evaluating the simulated AOD. **Fig. 7a–c** compare the mean AOD from the U50 km, V16 km, and V4 km configurations with the observations. The available sites include stations in the main downwind region as well as several background locations. Owing to the limited spatial coverage and data gaps, the regional evaluation includes all sites with valid observations during 13–18 March 2021. The three configurations capture the main dust-affected region and the associated downwind transport, but notable differences remain in the spatial distribution and magnitude of AOD. The U50 km simulation produces lower AOD than observed, with a smoother spatial pattern. With mesh refinement, the V16 km configuration exhibits a stronger AOD signal and improves the continuity of high AOD along the dust transport corridor. The V4 km configuration further enhances this continuity and better displays the spatial structure. These results indicate that mesh refinement affects not only the magnitude of AOD but also its spatial organization, with more pronounced changes in downwind regions. In particular, finer resolution enhances the spatial heterogeneity of AOD, producing sharper gradients and more distinct variations along the transport pathway. The smoother circulation and plume structures in the coarse-resolution simulation tend to broaden the transported dust layer and weaken AOD gradients along the transport pathway. With regional

https://doi.org/10.5194/egusphere-2026-3149
Preprint. Discussion started: 25 June 2026

refinement, improved representation of mesoscale flow variability and boundary-layer structure modifies the horizontal spreading and column-integrated distribution of dust, leading to sharper AOD gradients and a more organized downstream plume (Chen et al., 2013; Feng et al., 2023).

The scatterplot **(Fig. 7d)** provides a quantitative evaluation of the collocated observations and simulations. Correlations are high across the three configurations (r = 0.85-0.91), indicating that the model reproduces the spatial variability of AOD, whereas systematic biases decrease substantially with mesh refinement. The U50 km configuration shows a correlation coefficient of 0.87 but exhibits a substantial negative bias (NMB = –70.64%). The bias decreases markedly in V16 km (r = 0.85, NMB = –23.03%), and V4 km improves agreement with r = 0.91 and NMB = –19.01%. Overall, mesh refinement substantially reduces the underestimation of AOD while maintaining high spatial correlations with observations, indicating that the refined iAMAS configurations better capture column aerosol loading during this extreme East Asian dust event, with performance comparable to previous dust-model simulations and transport studies (Grini et al., 2005; Huneeus et al., 2011; Wu et al., 2019). The limited number of valid AERONET sites, especially over dust source regions, suggests that additional in situ and ground-based observations would help further constrain dust transport processes and optical properties.

3.2. Mechanisms driving the impacts of mesh refinement

Section 3.1 shows that different mesh configurations produce clear differences in the simulated surface PM_{10} concentration and AOD, especially in the magnitude and spatial organization of downwind dust plumes. These differences likely reflect the combined effects of dust emission, transport, and removal processes rather than a simple adjustment of total dust emission amount. The specific influence mechanisms responsible for these differences are examined below.

3.2.1. Dust emission sensitivity to regional mesh refinement

Dust emission is one of the main processes through which mesh refinement

https://doi.org/10.5194/egusphere-2026-3149
Preprint. Discussion started: 25 June 2026

influences the dust cycle, because it responds directly to resolution-dependent changes in surface wind stress (Kok et al., 2014). To quantify the sensitivity of dust emissions to horizontal resolution, we compared three simulations with different mesh configurations **(Table 3)**. Total dust emissions over East Asia during 13–17 March 2021 increase from 322.825 Tg in U50 km to 436.603 Tg in V16 km (+35.24%) and 500.301 Tg in V4 km (+54.98%). However, the magnitude of this sensitivity differs markedly among the major source regions. The dominant contribution comes from the MGD, where dust emissions increase from 140.841 Tg (U50 km) to 194.115 Tg (V16 km) and 232.920 Tg (V4 km), representing increases of 37.83% and 65.38%, respectively. Over the TKD, dust emissions rise from 72.401 Tg in U50 km to 102.021 Tg in V16 km and 105.412 Tg in V4 km, with relative increases of 40.91% and 45.59%, respectively. Other dust source regions, including the HC–WIM and LP, also exhibit increased emissions with mesh refinement, although their contributions are smaller than those from the MGD and TKD. The spatial distribution of mean dust emission flux further reveals where these emission increases are concentrated **(Fig. 8)**. The U50 km simulation produces broader and smoother dust emission belts, whereas V16 km and V4 km generate increasingly fragmented, filamentary, and band-shaped structures. Mesh refinement leads to greater local-scale heterogeneity in the HC–WIM and TKD, while the high-emission zones over the MGD become more pronounced and discontinuous. The difference maps further show that the strongest positive emission anomalies are concentrated along the southern Mongolian Plateau, indicating a consistent enhancement of emissions within the main dust source region.

These resolution-related changes in dust emission can influence the downstream distribution of transported dust by altering where and when dust is injected into the prevailing transport flows, rather than simply increasing the total emitted amount. Strong westerly and northwesterly flows during 13–16 March provided favorable pathways for eastward and southeastward dust transport from the major source regions to northern and eastern China **(Fig. 3)**. Under these circulation conditions, stronger emissions in the refined simulations are concentrated over upstream source

https://doi.org/10.5194/egusphere-2026-3149
Preprint. Discussion started: 25 June 2026

regions, especially the MGD and parts of the TKD and HC–WIM, allowing more dust to be injected into air masses that are efficiently transported downstream. This spatially heterogeneous enhancement may contribute to changes in dust plume intensity and spatial structure. The daily evolution of dust emissions further supports this interpretation. In the refined simulations, stronger and more localized emissions occur in upstream source regions during periods favorable for eastward and southeastward transport. For example, on 14 March, East Asian dust emissions increase from 118.788 Tg in U50 km to 163.987 Tg in V4 km, mainly due to the increase over the MGD from 69.978 to 102.158 Tg **(Figs. 3 and S2; Table S1)**. This coupling between the spatiotemporal evolution of emissions and the prevailing circulation helps explain how mesh refinement modifies the intensity and spatial organization of downstream dust transport through its influence on dust emissions.

The spatially heterogeneous enhancement and local intensification of emissions described above can be explained by the threshold-based and nonlinear response of the dust emission scheme to near-surface friction velocity. The S04 dust emission parameterization applied in this study triggers dust emission when the u^* exceeds a threshold value (u_t^*), and the resulting emission flux depends nonlinearly on the magnitude of this exceedance. Under such formulations, dust emission is controlled primarily by the high-stress tail of the near-surface wind distribution rather than by mean wind conditions (Shao, 2004; Kok et al., 2014; Mahowald et al., 2014). Mesh refinement can strengthen this high-stress tail by improving the representation of terrain gradients and land–surface transitions and by resolving localized flow accelerations, such as channeling and lee-side jets. It can also increase the spatial intermittency of surface stress associated with finer-scale flow structures, thereby enhancing the likelihood and intensity of threshold exceedance for dust emission (Jiménez and Dudhia, 2012; Feng et al., 2023). As a result, total dust emission can increase and become more spatially concentrated even without a proportional increase in exceedance frequency. This nonlinearity is examined in Section 3.2.2 through an analysis linking refinement-induced terrain effects to changes in the structure of u^*

https://doi.org/10.5194/egusphere-2026-3149
Preprint. Discussion started: 25 June 2026

and associated saltation exceedance metrics.

3.2.2. Impacts of mesh refinement on topography representation and wind friction velocity

Mesh refinement modifies dust emission and transport by altering terrain representation and the associated near-surface wind structure (Zender et al., 2003; Jiménez and Dudhia, 2012). **Fig. 9a–c** compares the terrain height simulated by the U50 km, V16 km, and V4 km configurations. With mesh refinement, the terrain exhibits enhanced elevation variability and sharper gradients, particularly along major mountain ranges, plateau margins, and basin boundaries. These changes are most evident over the Mongolian Plateau and across the complex topography of northwestern China. The corresponding difference maps **(Fig. 9d–f)** further show that mesh refinement modifies the resolved terrain structure. The difference between the V16 km and U50 km simulations **(Fig. 9d)** more clearly depicts steep terrain transitions and relief that are weakened by spatial averaging in the coarse-resolution mesh, especially along the margins of the Mongolian Plateau, the Tarim Basin, and the Tibetan Plateau. The difference between V4 km and U50 km **(Fig. 9e)** exhibits a similar but more pronounced pattern, reflecting a more detailed representation of local relief and finer-scale terrain variability. The comparison between V4 km and V16 km **(Fig. 9f)** indicates that further mesh refinement primarily sharpens existing terrain gradients and local relief, while the overall large-scale terrain configuration remains largely unchanged. To connect these terrain differences to low-level circulation linked to surface forcing, **Fig. S3** compares 850 hPa wind speed across the three meshes and their differences. The refined configurations show more spatially structured low-level wind-speed anomalies within the refinement region, consistent with the refinement-induced changes in u^* discussed below.

Consistent with these resolution-dependent differences in terrain and low-level winds, u^* also reveals systematic changes in its spatial structure **(Fig. 10)**. Relative to the U50 km simulation, both the V16 km and V4 km configurations exhibit a finer spatial structure of u^*, with sharper gradients and more localized regions of elevated

https://doi.org/10.5194/egusphere-2026-3149
Preprint. Discussion started: 25 June 2026

values. At the V4 km resolution, these localized high-u^* features are more clearly expressed, whereas they appear spatially smoothed and diffused at coarser resolution. This indicates that mesh refinement enhances the spatial variability of near-surface wind forcing, which is a key driver of dust emission. In our study, emission is more strongly influenced by episodic strong wind events than by mean wind conditions, reflecting the nonlinear dependence of emission flux on exceedances of friction velocity above the saltation threshold (Shao, 2004). To quantify this nonlinear response, we analyzed the saltation occurrence frequency ($f_{saltation}$) and a diagnostic metric S_3, defined as the regional mean cubic exceedance of friction velocity above the saltation threshold. The cubic weighting emphasizes intense exceedances of u^*, consistent with the nonlinear dependence of dust emission flux on friction velocity in threshold-based dust emission schemes, and therefore better captures the contribution of episodic strong-wind events than occurrence frequency alone (Zender et al., 2003; Shao, 2004; Klose & Shao, 2012; Kok et al., 2014). In **Fig. 11**, both $f_{saltation}$ and S_3 are normalized by their U50 km values to show the relative changes caused by mesh refinement. Across the main dust source regions, $f_{saltation}$ generally decreases with mesh refinement, with reductions of 2-22% in the V16 km simulation and 14-36% in the V4 km simulation relative to U50 km. In contrast, S_3 increases consistently in the dust source regions, by 4-42% in V16 km and by 31-76% in V4 km. The largest increases occur over the MGD and HC–WIM in the V4 km simulation, reaching 57% and 76%, respectively, despite only moderate decreases in $f_{saltation}$ **(Fig. 11)**.

The opposite responses of $f_{saltation}$ and S_3 provide a reasonable explanation for the apparent contrast between increasing region-integrated dust emissions **(Table 3)** and decreasing saltation occurrence frequency in some regions **(Fig. 11)**. Under mesh refinement, u^* exceedances above u_t^* become more spatially concentrated and higher in amplitude, leading to a stronger contribution from the upper tail of the u^* distribution. Thus, total dust emission can increase even when saltation occurs less frequently in an area-averaged sense. Similar patterns have been widely documented in both observational and modeling studies of dust emission, highlighting the

https://doi.org/10.5194/egusphere-2026-3149
Preprint. Discussion started: 25 June 2026

dominant role of extreme wind events in threshold-controlled systems (Marsham et al., 2011; Kok, 2011; Klose & Shao, 2012).

3.2.3. Impacts of regional refinement on dust mass loading

Dust mass loading reflects the integrated effects of dust emission, transport, and removal processes, and therefore provides a useful measure of the net response of the dust burden to regional mesh refinement (Huneeus et al., 2011). The spatial distributions in **Fig. 12a–c** show that dust mass loading is primarily concentrated along the main west–east transport corridor downstream of the source regions, with broadly similar large-scale patterns across the three simulations. Differences among the simulations are mainly reflected in the spatial coverage and magnitude of enhanced dust loading. The daily evolution of dust mass loading in **Fig. S4** indicates that the timing and large-scale progression are generally consistent, while regional differences in intensity persist. The difference maps further reveal that both the V16 km and V4 km simulations tend to produce higher dust loading than U50 km across several downwind regions **(Fig. 12d–e)**. By contrast, the difference between V4 km and V16 km is characterized by localized positive and negative anomalies **(Fig. 12f)**. Overall, these results indicate that the response of dust mass loading to mesh refinement is spatially heterogeneous.

To further quantify the impact of mesh refinement on atmospheric dust mass loading, we calculated region-integrated dust mass loading during 13–17 March 2021 **(Table 4)**. Across East Asia, region-integrated dust mass loading increases with resolution, from 75.094 Tg in U50 km to 85.394 Tg in V16 km (+13.72%) and 92.744 Tg in V4 km (+23.50%) **(Table 4)**. Despite the overall increase across East Asia, the regional response is not spatially uniform. At the regional scale, the largest relative increases occur over the NCP, where dust mass loading rises from 3.897 Tg in U50 km to 5.592 Tg in V16 km (+43.49%) and 6.378 Tg in V4 km (+63.66%) **(Table 4)**. In contrast, over the LP and YRD, V16 km produces slightly higher dust loading than U50 km, with increases of +7.62% and +7.69%, respectively, whereas V4 km yields lower values than U50 km, with decreases of −5.18% and −30.49%, respectively.

https://doi.org/10.5194/egusphere-2026-3149
Preprint. Discussion started: 25 June 2026

These regional contrasts indicate that mesh refinement does not simply produce a uniform increase in dust loading, but instead modifies its regional distribution. A similar pattern is also found in the regional mean surface PM_{10} concentration over the YRD **(Table S2)**, where V16 km increases from 18.667 μg m^{-3} in U50 km to 43.437 μg m^{-3} (+132.70%), whereas V4 km decreases to 13.481 μg m^{-3} (−27.78%). The consistent decrease in both column dust mass loading and surface PM_{10} indicates that the reduced dust burden over the YRD in V4 km is also reflected near the surface.

Regional differences in dust mass loading reflect the combined effects of the spatiotemporal emission changes and transport structures discussed in Section 3.2.1. Mesh refinement enhances dust emissions over major upstream source regions, thereby changing when and where dust becomes available for subsequent transport. The circulation fields show a broadly similar synoptic evolution across the three simulations, with persistent westerly and northwesterly flows during 13−16 March providing favorable pathways for dust transport from the MGD, TKD, and HC−WIM toward northern and eastern China **(Figs. 3 and S1)**. Within this circulation background, the 850 hPa wind-speed differences indicate that mesh refinement modifies the spatial structure and local intensity of the transport flow within the refinement region, especially along the pathway from the source regions to downwind areas **(Fig. S3)**. This more spatially structured transport flow facilitates dust transport from upstream source regions and helps shape the eastward and southeastward extension of the dust plume. Consistently, the distribution of daily dust mass loading shows that the main dust plume develops over the source regions during 14−16 March and is subsequently transported eastward along the prevailing flow, with stronger and more spatially organized loading in the refined simulations **(Fig. S4)**. Therefore, the enhanced dust loading over the NCP likely reflects the combined influence of stronger upstream emissions and more organized transport flow from the MGD, TKD, and HC−WIM. In contrast, the concurrent decreases in both dust mass loading and surface PM_{10} concentration over the YRD in the V4 km simulation suggest that the reduced dust burden may not be explained by emission distribution and transport differences

https://doi.org/10.5194/egusphere-2026-3149
Preprint. Discussion started: 25 June 2026

alone, but may also involve enhanced removal processes. Thus, the role of wet scavenging in modulating downwind dust loading, particularly over the YRD, is further examined in Section 3.2.4.

3.2.4. Impacts of regional mesh refinement on dust wet scavenging

Dust wet scavenging represents an important removal process that can alter downstream dust loading by removing transported dust, especially over eastern China. Here we focus on the contrast between U50 km and V4 km, because this comparison most clearly illustrates resolution-dependent differences in precipitation structure and associated wet scavenging. **Fig. 13** shows that the two simulations produce broadly similar total precipitation patterns, with the main precipitation band extending across southern and eastern China. However, the V4 km simulation exhibits stronger spatial variability and more localized precipitation anomalies. Compared with U50 km, the V4 km configuration produces increased precipitation over parts of southern and eastern China, including the YRD, while precipitation decreases over some regions of central and northern China **(Fig. 13c)**. The spatial distribution of dust wet scavenging further illustrates how precipitation differences, together with the distribution of transported dust, modulate dust removal. The V4 km simulation produces stronger dust wet scavenging over the YRD than U50 km **(Fig. 13d−f)**, indicating a localized enhancement of dust removal in this downwind region.

Table 5 further quantifies the regional differences in wet scavenging rate and total dust wet scavenging across the analyzed regions. From U50 km to V4 km, the dust wet scavenging rate decreases from 158.554 to 77.663 mg m^{-2} day^{-1} over the TKD and from 74.261 to 15.966 mg m^{-2} day^{-1} over the HC−WIM, indicating weaker regional-mean wet removal over dust source regions. In these regions, the increased dust mass loading in V4 km is therefore more consistent with the dominant influence of enhanced emissions and circulation-driven transport, as discussed in Sects. 3.2.1-3.2.3, rather than with wet scavenging. By contrast, over the downwind YRD, the wet scavenging rate increases from 11.117 to 25.041 mg m^{-2} day^{-1}, and the total dust wet scavenging increases from 0.014 to 0.033 Tg. This enhanced removal

https://doi.org/10.5194/egusphere-2026-3149
Preprint. Discussion started: 25 June 2026

coincides with the 30.49% reduction in dust mass loading over the YRD in V4 km relative to U50 km **(Table 4)**. The V16 km simulation does not show such an enhancement over the YRD, with a wet scavenging rate of 10.865 mg m^{-2} day^{-1} and total wet scavenging of 0.015 Tg, both close to the U50 km values **(Table S3)**. The stronger wet scavenging over the YRD in V4 km than in V16 km suggests that the higher downstream resolution in the V4 km mesh configuration may exert a stronger influence on precipitation structure, thereby leading to a more pronounced effect on dust wet removal along the transport pathway. Wet scavenging therefore acts as a removal pathway superimposed on the emission- and transport-driven redistribution of dust. While enhanced emissions and modified circulation-influenced transport largely explain the increased dust loading over source and near-source regions, stronger wet scavenging over the YRD can locally offset the transported dust burden and contribute to the altered downstream dust distribution. This finding further implies that, when precipitation occurs along downwind transport pathways, extending the convection-permitting refinement region to cover these areas may help better represent dust–cloud–precipitation interactions, which warrants further investigation in future work.

4. Conclusions

In this study, we applied the global variable-resolution modeling framework iAMAS (v2.6.3), coupled with a sectional dust module, to simulate the extreme East Asian dust storm during 13–18 March 2021 and assess the impacts of source-region mesh refinement. This is the first attempt to reproduce a strong East Asian dust outbreak using a global variable-resolution mesh model with convection-permitting scale refinement over the major source regions. Based on a globally quasi-uniform 50 km configuration (U50 km) and two regionally refined meshes (V16 km and V4 km), iAMAS reproduces the reanalysis-constrained synoptic evolution of this dust event, including the large-scale trough-ridge pattern and the associated surface pressure distribution. Increasing mesh resolution allows a more detailed representation of

https://doi.org/10.5194/egusphere-2026-3149
Preprint. Discussion started: 25 June 2026

terrain and its dynamical influence on near-surface winds. As a result, terrain-modulated flow features, such as topographically confined wind corridors and sharpened wind gradients across key orographic transitions, are more clearly resolved. These resolution-dependent dynamical changes contribute to substantial differences in simulated dust emission and transport, with total dust emissions over East Asia increasing by 35.24% in V16 km and 54.98% in V4 km relative to U50 km.

Comparisons with NOAA 10-m wind observations indicate that the refined meshes better capture the spatial heterogeneity and temporal variability of daily mean wind speed, with regional correlations reaching 0.81-0.92 in V4 km and source-region wind-speed biases substantially reduced. Consistent with the improved near-surface dynamics, iAMAS also reproduces the observed PM_{10} evolution over eastern China and the associated dust transport corridor. The refined meshes produce sharper concentration gradients and a clearer spatial distribution along the transport pathway, with the V4 km simulation showing the strongest agreement with PM_{10} observations, including a correlation of 0.85 and an NMB below 20%. By contrast, the U50 km simulation generates smoother dust plumes and weaker peak concentrations. This likely reflects its coarser representation of terrain-flow interactions and friction velocity, which underestimates the nonlinear contribution from strong friction-velocity events above the emission threshold. Evaluation against AERONET AOD further shows that column aerosol loading is better represented under mesh refinement, with the V4 km simulation exhibiting improved agreement with observations in both magnitude and spatial distribution across stations.

Overall, the benefits of regional mesh refinement arise from three interacting effects: (i) improved representation of terrain–flow coupling, which intensifies localized extremes in friction velocity and strengthens threshold-controlled dust emission; (ii) modification of dust transport pathways due to the combined effects of spatiotemporal emission changes and resolution-dependent circulation changes, leading to spatial redistribution of dust loading rather than a uniform increase; and (iii) resolution dependence of precipitation structure, which can locally offset emission-

https://doi.org/10.5194/egusphere-2026-3149
Preprint. Discussion started: 25 June 2026

and transport-driven increases in dust mass loading through wet scavenging. Region-integrated dust mass loading over East Asia increases by 13.72 % in V16 km and 23.50 % in V4 km relative to U50 km. The response is stronger over the NCP, where dust loading increases by 43.49 % in V16 km and 63.66 % in V4 km. However, the response is not spatially uniform. In humid downstream regions such as the YRD, the V4 km simulation produces stronger localized wet scavenging and reduces dust loading by 30.49% relative to U50 km. This competition between dynamical forcing from emission and transport and wet scavenging suggests that the impact of mesh refinement on dust burden is strongly region dependent.

These findings motivate further assessment of how robust these resolution effects are across additional strong dust events and under alternative model settings. Because this study focuses on a single extreme dust event, the relative roles of terrain-induced wind variability, circulation-related transport pathways, and precipitation-related removal may depend on the prevailing synoptic conditions and regional hydrometeorological environment. In particular, future work is needed to examine the sensitivity to dust emission schemes and mesh refinement under different synoptic conditions, and to better quantify how these processes jointly affect regional dust emission and long-range transport. Such assessments will provide a stronger basis for applying global variable-resolution models to event-scale dust prediction and to the evaluation of multiple dust emission schemes.

https://doi.org/10.5194/egusphere-2026-3149
Preprint. Discussion started: 25 June 2026

Code availability.

The used version of the iAMAS model is openly available at Zenodo (https://doi.org/10.5281/zenodo.20115846).

Data availability.

ERA5 reanalysis data are available from the Copernicus Climate Data Store (https://cds.climate.copernicus.eu/). Surface PM_{10} concentration data can be accessed through the China National Environmental Monitoring Centre (CNEMC; https://www.cnemc.cn/). Surface wind speed observations were obtained from NOAA station observations compiled in the Global Surface Summary of the Day (GSOD) dataset (https://www.ncei.noaa.gov/). Column-integrated aerosol loading was evaluated using sun-photometer observations from the Aerosol Robotic Network (AERONET). The AERONET Version 3 Direct-Sun AOD products at Level 2.0 and Level 1.5 are available from the AERONET website (https://aeronet.gsfc.nasa.gov/).

Author contributions.

YX, CZ, and JF designed the experiments and developed the methodology. YX, JF, XQ, and ZX contributed to software implementation. YX and CZ performed the analysis and data curation, with contributions from XZ. JZ, ZY, QY, GL, and ZZ contributed to the investigation. The manuscript draft was written by YX and CZ. CZ supervised the study. All authors reviewed and edited the manuscript.

Competing interests.

The contact author has declared that none of the authors has any competing interests.

Disclaimer.

Publisher's note: Copernicus Publications remains neutral with regard to

https://doi.org/10.5194/egusphere-2026-3149
Preprint. Discussion started: 25 June 2026

jurisdictional claims made in the text, published maps, institutional affiliations, or any other geographical representation in this paper. While Copernicus Publications makes every effort to include appropriate place names, the final responsibility lies with the authors.

Acknowledgments.

This work used computing resources from the Supercomputing Center of the University of Science and Technology of China (USTC), the National Key Scientific and Technological Infrastructure project "Earth System Numerical Simulation Facility" (EarthLab), and the Qingdao Supercomputing and Big Data Center.

Financial support.

This work was supported by the National Natural Science Foundation of China (NSFC) under the Youth Student Basic Research Project (grant no. 425B2031), the Strategic Priority Research Program of the Chinese Academy of Sciences (grant no. XDB0500303), the National Natural Science Foundation of China (grant no. 41775146), the USTC Research Funds of the Double First-Class Initiative (grant nos. YD2080002007 and KY2080000114), the Science and Technology Innovation Project of Laoshan Laboratory (grant no. LSKJ202300305), and the Cultivation Plan for Tianshan Talent Scholar, China (grant no. 2022TSYCCX0012).

https://doi.org/10.5194/egusphere-2026-3149
Preprint. Discussion started: 25 June 2026

References

Adebiyi, A. A., and Kok, J. F.: Climate models miss most of the coarse dust in the atmosphere, Sci. Adv., 6, eaaz9507, https://doi.org/10.1126/sciadv.aaz9507, 2020.

Alfaro, S. C., and Gomes, L.: Modeling mineral aerosol production by wind erosion: Emission intensities and aerosol size distributions in source areas, J. Geophys. Res.-Atmos., 106, 18075-18084, https://doi.org/10.1029/2000JD900339, 2001.

Chappell, A., Hennen, M., Schepanski, K., Dhital, S., and Tong, D.: Reducing resolution dependency of dust emission modeling using albedo-based wind friction, Geophys. Res. Lett., 51, e2023GL106540, https://doi.org/10.1029/2023GL106540, 2024.

Chen, F., and Dudhia, J.: Coupling an advanced land surface-hydrology model with the Penn State-NCAR MM5 modeling system. Part I: Model implementation and sensitivity, Mon. Weather Rev., 129, 569-585, https://doi.org/10.1175/1520-0493(2001)129%3C0569:CAALSH%3E2.0.CO;2, 2001.

Chen, S., Huang, J., Zhao, C., Qian, Y., Leung, L. R., and Yang, B.: Modeling the transport and radiative forcing of Taklimakan dust over the Tibetan Plateau: A case study in the summer of 2006, J. Geophys. Res.-Atmos., 118, 797-812, https://doi.org/10.1002/jgrd.50122, 2013.

Feng, J., Zhao, C., Du, Q., Xu, M., Gu, J., Hu, Z., and Chen, Y.: Simulating atmospheric dust with a global variable-resolution model: Model description and impacts of mesh refinement, J. Adv. Model. Earth Syst., 15, e2023MS003636, https://doi.org/10.1029/2023MS003636, 2023.

Feng, J., Zhao, C., Gu, J., Li, G., Xu, M., Lin, S., and Feng, J.: Dust impacts on the Indian summer monsoon: chaotic or physical effect?, Atmos. Chem. Phys., 25, 12051-12068, https://doi.org/10.5194/acp-25-12051-2025, 2025.

Giles, D. M., Sinyuk, A., Sorokin, M. G., Schafer, J. S., Smirnov, A., Slutsker, I., Eck, T. F., Holben, B. N., Lewis, J. R., Campbell, J. R., Welton, E. J., Korkin, S. V., and Lyapustin, A. I.: Advancements in the Aerosol Robotic Network (AERONET) Version 3 database-Automated near-real-time quality control algorithm with improved cloud screening for Sun photometer aerosol optical depth (AOD) measurements, Atmos. Meas. Tech., 12, 169-209, https://doi.org/10.5194/amt-12-169-2019, 2019.

Grell, G. A., and Freitas, S. R.: A scale and aerosol aware stochastic convective parameterization for weather and air quality modeling, Atmos. Chem. Phys., 14, 5233-5250, https://doi.org/10.5194/acp-14-5233-2014, 2014.

Grini, A., Myhre, G., Zender, C. S., and Isaksen, I. S. A.: Model simulations of dust sources and transport in the global atmosphere: Effects of soil erodibility and wind speed variability, J. Geophys. Res.-Atmos., 110, D02205, https://doi.org/10.1029/2004JD005037, 2005.

Gu, J., Feng, J., Hao, X., Fang, T., Zhao, C., An, H., Chen, J., Xu, M., Li, J., Han, W., Yang, C., Li, F., and Chen, D.: Establishing a non-hydrostatic global atmospheric modeling system at 3-km horizontal resolution with aerosol feedbacks on the Sunway supercomputer of China, Sci. Bull., 67, 1170-1181, https://doi.org/10.1016/j.scib.2022.03.009, 2022.

https://doi.org/10.5194/egusphere-2026-3149
Preprint. Discussion started: 25 June 2026

940 Gu, J., Zhao, C., Xu, M., Ma, Y., Hu, Z., Jin, C., Guo, J., Geng, T., and Cai, W.: Fast
941 warming over the Mongolian Plateau a catalyst for extreme rainfall over North China,
942 Geophys. Res. Lett., 52, e2024GL113737, https://doi.org/10.1029/2024GL113737, 2025.
943 Heinold, B., Knippertz, P., Marsham, J. H., Fiedler, S., Dixon, N. S., Schepanski, K., Laurent,
944 B., and Tegen, I.: The role of deep convection and nocturnal low-level jets for dust
945 emission in summertime West Africa: Estimates from convection-permitting simulations,
946 J. Geophys. Res.-Atmos., 118, 4385-4400, https://doi.org/10.1002/jgrd.50402, 2013.
947 Hersbach, H., Bell, B., Berrisford, P., Hirahara, S., Horányi, A., Muñoz-Sabater, J., Nicolas,
948 J., Peubey, C., Radu, R., Schepers, D., Simmons, A., Soci, C., Abdalla, S., Abellan, X.,
949 Balsamo, G., Bechtold, P., Biavati, G., Bidlot, J., Bonavita, M., De Chiara, G., Dahlgren,
950 P., Dee, D., Diamantakis, M., Dragani, R., Flemming, J., Forbes, R., Fuentes, M., Geer,
951 A., Haimberger, L., Healy, S., Hogan, R. J., Hólm, E., Janisková, M., Keeley, S.,
952 Laloyaux, P., Lopez, P., Lupu, C., Radnoti, G., de Rosnay, P., Rozum, I., Vamborg, F.,
953 Villaume, S., and Thépaut, J.-N.: The ERA5 global reanalysis, Q. J. Roy. Meteor. Soc.,
954 146, 1999-2049, https://doi.org/10.1002/qj.3803, 2020.
955 Hong, S. Y., Noh, Y., and Dudhia, J.: A new vertical diffusion package with an explicit
956 treatment of entrainment processes, Mon. Weather Rev., 134, 2318-2341,
957 https://doi.org/10.1175/MWR3199.1, 2006.
958 Hu, Z., Huang, J., Zhao, C., Ma, Y., Jin, Q., Qian, Y., Leung, L. R., Bi, J., and Ma, J.:
959 Trans-Pacific transport and evolution of aerosols: Spatiotemporal characteristics and
960 source contributions, Atmos. Chem. Phys., 19, 12709-12730,
961 https://doi.org/10.5194/acp-19-12709-2019, 2019.
962 Huang, X., Rhoades, A. M., Ullrich, P. A., and Zarzycki, C. M.: An evaluation of the
963 variable-resolution CESM for modeling California's climate, J. Adv. Model. Earth Syst.,
964 8, 345-369, https://doi.org/10.1002/2015MS000559, 2016.
965 Huneeus, N., Schulz, M., Balkanski, Y., Griesfeller, J., Prospero, J., Kinne, S., Bauer, S.,
966 Boucher, O., Chin, M., Dentener, F., Diehl, T., Easter, R., Fillmore, D., Ghan, S.,
967 Ginoux, P., Grini, A., Horowitz, L., Koch, D., Krol, M. C., Landing, W., Liu, X.,
968 Mahowald, N., Miller, R., Morcrette, J.-J., Myhre, G., Penner, J., Perlwitz, J., Stier, P.,
969 Takemura, T., and Zender, C. S.: Global dust model intercomparison in AeroCom phase
970 I, Atmos. Chem. Phys., 11, 7781-7816, https://doi.org/10.5194/acp-11-7781-2011, 2011.
971 Huo, Q., Yin, Z., Ma, X., and Wang, H.: Distinctive dust weather intensities in North China
972 resulted from two types of atmospheric circulation anomalies, Atmos. Chem. Phys., 25,
973 1711-1724, https://doi.org/10.5194/acp-25-1711-2025, 2025.
974 Iacono, M. J., Delamere, J. S., Mlawer, E. J., Shephard, M. W., Clough, S. A., and Collins, W.
975 D.: Radiative forcing by long-lived greenhouse gases: Calculations with the AER
976 radiative transfer models, J. Geophys. Res.-Atmos., 113, D13103,
977 https://doi.org/10.1029/2008JD009944, 2008.
978 IPCC: Climate Change 2021: The Physical Science Basis. Contribution of Working Group I
979 to the Sixth Assessment Report of the Intergovernmental Panel on Climate Change,
980 Cambridge University Press, https://doi.org/10.1017/9781009157896, 2023.
981 Idrissa, N. F., Zhao, C., Hu, Z., Feng, J., and Du, Q.: Long-range transport impact of a severe
982 dust storm over the Yangtze River Basin region and its modeling sensitivity to dust

https://doi.org/10.5194/egusphere-2026-3149
Preprint. Discussion started: 25 June 2026

emission scheme, Atmos. Res., 310, 107612, https://doi.org/10.1016/j.atmosres.2024.107612, 2024.

Jickells, T. D., An, Z. S., Andersen, K. K., Baker, A. R., Bergametti, G., Brooks, N., Cao, J. J., Boyd, P. W., Duce, R. A., Hunter, K. A., Kawahata, H., Kubilay, N., laRoche, J., Liss, P. S., Mahowald, N., Prospero, J. M., Ridgwell, A. J., Tegen, I., and Torres, R.: Global iron connections between desert dust, ocean biogeochemistry, and climate, Science, 308, 67-71, https://doi.org/10.1126/science.1105959, 2005.

Jiménez, P. A., and Dudhia, J.: Improving the representation of resolved and unresolved topographic effects on surface wind in the WRF model, J. Appl. Meteorol. Clim., 51, 300-316, https://doi.org/10.1175/JAMC-D-11-084.1, 2012.

Ju, L., Ringler, T., and Gunzburger, M.: Voronoi tessellations and their application to climate and global modeling, in: Numerical techniques for global atmospheric models, edited by: Lauritzen, P. H., Jablonowski, C., Taylor, M. A., and Nair, R. D., Springer, 313-342, https://doi.org/10.1007/978-3-642-11640-7_10, 2011.

Kang, J. Y., Yoon, S. C., Shao, Y., and Kim, S. W.: Comparison of vertical dust flux by implementing three dust emission schemes in WRF/Chem, J. Geophys. Res.-Atmos., 116, D09202, https://doi.org/10.1029/2010JD014649, 2011.

Klose, M., and Shao, Y.: Stochastic parameterization of dust emission and application to convective atmospheric conditions, Atmos. Chem. Phys., 12, 7309-7320, https://doi.org/10.5194/acp-12-7309-2012, 2012.

Kok, J. F.: A scaling theory for the size distribution of emitted dust aerosols suggests climate models underestimate the size of the global dust cycle, P. Natl. Acad. Sci. USA, 108, 1016-1021, https://doi.org/10.1073/pnas.1014798108, 2011.

Kok, J. F., Mahowald, N. M., Fratini, G., Gillies, J. A., Ishizuka, M., Leys, J. F., Mikami, M., Park, M. S., Park, S. U., Van Pelt, R. S., and Zobeck, T. M.: An improved dust emission model-Part 1: Model description and comparison against measurements, Atmos. Chem. Phys., 14, 13023-13041, https://doi.org/10.5194/acp-14-13023-2014, 2014.

Kok, J. F., Ridley, D. A., Zhou, Q., Miller, R. L., Zhao, C., Heald, C. L., Ward, D. S., Albani, S., and Haustein, K.: Smaller desert dust cooling effect estimated from analysis of dust size and abundance, Nat. Geosci., 10, 274-278, https://doi.org/10.1038/ngeo2912, 2017.

Konaré, A., Zakey, A. S., Solmon, F., Giorgi, F., Rauscher, S., Ibrah, S., and Bi, X.: A regional climate modeling study of the effect of desert dust on the West African monsoon, J. Geophys. Res.-Atmos., 113, D12206, https://doi.org/10.1029/2007JD009322, 2008.

Laprise, R.: Regional climate modelling, J. Comput. Phys., 227, 3641-3666, https://doi.org/10.1016/j.jcp.2006.10.024, 2008.

Li, G., Zhao, C., Gu, J., Feng, J., Xu, M., Hao, X., Chen, J., An, H., Cai, W., and Geng, T.: Excessive equatorial light rain causes modeling dry bias of Indian summer monsoon rainfall, npj Clim. Atmos. Sci., 8, 23, https://doi.org/10.1038/s41612-025-00916-1, 2025.

Li, G., Zhao, C., Xu, M., Feng, J., Zhong, L., Li, R., and Fu, Y.: Simulating moisture transport over the Tibetan Plateau in summer of 2015 across scales with a global variable-resolution model (MPAS-A), J. Geophys. Res.-Atmos., 129, e2023JD040205, https://doi.org/10.1029/2023JD040205, 2024.

https://doi.org/10.5194/egusphere-2026-3149
Preprint. Discussion started: 25 June 2026

Mahowald, N. M., Albani, S., Kok, J. F., Engelstaedter, S., Scanza, R., Ward, D. S., and Flanner, M. G.: The size distribution of desert dust aerosols and its impact on the Earth system, Aeolian Res., 15, 53 – 71, https://doi.org/10.1016/j.aeolia.2013.09.002, 2014.

Marsham, J. H., Knippertz, P., Dixon, N. S., Parker, D. J., and Lister, G. M. S.: The importance of the representation of deep convection for modeled dust-generating winds over West Africa during summer, Geophys. Res. Lett., 38, L16803, https://doi.org/10.1029/2011GL048368, 2011.

Mlawer, E. J., Taubman, S. J., Brown, P. D., Iacono, M. J., and Clough, S. A.: Radiative transfer for inhomogeneous atmospheres: RRTM, a validated correlated-k model for the longwave, J. Geophys. Res.-Atmos., 102, 16663-16682, https://doi.org/10.1029/97JD00237, 1997.

Owen, P. R.: Saltation of uniform grains in air, J. Fluid Mech., 20, 225-242, https://doi.org/10.1017/S0022112064001173, 1964.

Pérez, C., Nickovic, S., Baldasano, J. M., Sicard, M., Rocadenbosch, F., and Cachorro, V. E.: A long Saharan dust event over the western Mediterranean: Lidar, sun photometer observations, and regional dust modeling, J. Geophys. Res.-Atmos., 111, D15214, https://doi.org/10.1029/2005JD006579, 2006.

Rauscher, S. A., Ringler, T. D., Skamarock, W. C., and Mirin, A. A.: Exploring a global multiresolution modeling approach using aquaplanet simulations, J. Climate, 26, 2432-2452, https://doi.org/10.1175/JCLI-D-12-00154.1, 2013.

Ringler, T., Ju, L., and Gunzburger, M.: A multiresolution method for climate system modeling: Application of spherical centroidal Voronoi tessellations, Ocean Dynam., 58, 475-498, https://doi.org/10.1007/s10236-008-0157-2, 2008.

Ringler, T., Thuburn, J., Klemp, J. B., and Skamarock, W. C.: A unified approach to energy conservation and potential vorticity dynamics for arbitrarily structured C-grids, J. Comput. Phys., 229, 3065-3090, https://doi.org/10.1016/j.jcp.2009.12.007, 2010.

Shao, Y.: A model for mineral dust emission, J. Geophys. Res.-Atmos., 106, 20239-20254, https://doi.org/10.1029/2001JD900171, 2001.

Shao, Y.: Simplification of a dust emission scheme and comparison with data, J. Geophys. Res.-Atmos., 109, D10202, https://doi.org/10.1029/2003JD004372, 2004.

Shao, Y., Ishizuka, M., Mikami, M., and Leys, J. F.: Parameterization of size-resolved dust emission and validation with measurements, J. Geophys. Res.-Atmos., 116, D08203, https://doi.org/10.1029/2010JD014527, 2011.

Shao, Y., and Lu, H.: A simple expression for wind erosion threshold friction velocity, J. Geophys. Res.-Atmos., 105, 22437-22443, https://doi.org/10.1029/2000JD900304, 2000.

Shao, Y., Raupach, M. R., and Findlater, P. A.: The effect of saltation bombardment on the entrainment of dust by wind, J. Geophys. Res., 98, 12719-12726, https://doi.org/10.1029/93JD00396, 1993.

Shin, S. K., Tesche, M., Noh, Y., and Müller, D.: Aerosol-type classification based on AERONET version 3 inversion products, Atmos. Meas. Tech., 12, 3789-3803, https://doi.org/10.5194/amt-12-3789-2019, 2019.

Skamarock, W. C., Klemp, J. B., Duda, M. G., Fowler, L. D., Park, S.-H., and Ringler, T. D.: A multiscale nonhydrostatic atmospheric model using centroidal Voronoi tessellations

https://doi.org/10.5194/egusphere-2026-3149
Preprint. Discussion started: 25 June 2026

and C-grid staggering, Mon. Weather Rev., 140, 3090-3105, https://doi.org/10.1175/MWR-D-11-00215.1, 2012.

Sun, H., Pan, Z., and Liu, X.: Numerical simulation of spatial-temporal distribution of dust aerosol and its direct radiative effects on East Asian climate, J. Geophys. Res.-Atmos., 117, D13206, https://doi.org/10.1029/2011JD017219, 2012.

Thompson, G., Field, P. R., Rasmussen, R. M., and Hall, W. D.: Explicit forecasts of winter precipitation using an improved bulk microphysics scheme. Part II: Implementation of a new snow parameterization, Mon. Weather Rev., 136, 5095-5115, https://doi.org/10.1175/2008MWR2387.1, 2008.

Thuburn, J., Ringler, T. D., Skamarock, W. C., and Klemp, J. B.: Numerical representation of geostrophic modes on arbitrarily structured C-grids, J. Comput. Phys., 228, 8321-8335, https://doi.org/10.1016/j.jcp.2009.08.006, 2009.

Tobías, A., Querol, X., Roqué, M., Suu Lwin, K., Yuan, L., Ith, S., Zin Wai, H., Lester Chua, P., Solá, I., Renzi, M., Stafoggia, M., and Hashizume, M.: Short-term exposure to desert dust and sandstorms and all-cause and cause-specific mortality and morbidity: A systematic review and meta-analysis, Environ. Int., 196, 109277, https://doi.org/10.1016/j.envint.2025.109277, 2025.

Woodage, M. J., Slingo, A., Woodward, S., and Comer, R. E.: U.K. HiGEM: Simulations of desert dust and biomass burning aerosols with a high-resolution atmospheric GCM, J. Climate, 23, 1636-1659, https://doi.org/10.1175/2009JCLI2994.1, 2010.

Wu, C., Lin, Z., He, J., Zhang, M., Liu, X., Zhang, R., and Brown, H.: A process-oriented evaluation of dust emission parameterizations in CESM: Simulation of a typical severe dust storm in East Asia, J. Adv. Model. Earth Syst., 8, 1432-1452, https://doi.org/10.1002/2016MS000723, 2016.

Wu, C., Lin, Z., Shao, Y., Liu, X., and Li, Y.: Drivers of recent decline in dust activity over East Asia, Nat. Commun., 13, 7105, https://doi.org/10.1038/s41467-022-34823-3, 2022.

Wu, M., Liu, X., Yang, K., Luo, T., Wang, Z., Wu, C., Zhang, K., Yu, H., and Darmenov, A.: Modeling dust in East Asia by the Community Earth System Model (CESM) and sources of biases, J. Geophys. Res.-Atmos., 124, 8043-8064, https://doi.org/10.1029/2019JD030799, 2019.

Xue, Y., Zhang, X., Lei, J., Li, S., Liu, L., Wang, Z., Tian, W., Tang, X., and Chen, X.: East Asian dust storm in March 2021: Perspective views from ground observation, satellite measurement and numerical simulation, Atmos. Environ., 350, 121152, https://doi.org/10.1016/j.atmosenv.2025.121152, 2025.

Xu, M., Zhao, C., Gu, J., Feng, J., Li, G., and Guo, J.: Appropriately representing convective heating is critical for predicting catastrophic heavy rainfall in 2021 in Henan Province of China, Environ. Res. Commun., 5, 051002, https://doi.org/10.1088/2515-7620/accfec, 2023.

Xu, M., Zhao, C., Li, G., Gu, J., Feng, J., Zhang, Z., and Guo, J.: Modeling across scales of heavy precipitation with a global variable-resolution model: A case study of a catastrophic event in China, J. Geophys. Res.-Atmos., 129, e2024JD041180, https://doi.org/10.1029/2024JD041180, 2024.

https://doi.org/10.5194/egusphere-2026-3149
Preprint. Discussion started: 25 June 2026

Zarzycki, C. M., and Jablonowski, C.: A multidecadal simulation of Atlantic tropical cyclones using a variable-resolution global model, J. Adv. Model. Earth Syst., 6, 805-828, https://doi.org/10.1002/2014MS000352, 2014.

Zender, C. S., Bian, H., and Newman, D.: Mineral dust entrainment and deposition (DEAD) model: Description and 1990s dust climatology, J. Geophys. Res.-Atmos., 108, 4416, https://doi.org/10.1029/2002JD002775, 2003.

Zhao, C., Liu, X., Leung, L. R., Johnson, B., McFarlane, S. A., Gustafson, W. I., Jr., Fast, J. D., and Easter, R.: The spatial distribution of mineral dust and its shortwave radiative forcing over North Africa: Modeling sensitivities to dust emissions and aerosol size treatments, Atmos. Chem. Phys., 10, 8821-8838, https://doi.org/10.5194/acp-10-8821-2010, 2010.

Zhao, C., Liu, X., Leung, L. R., and Hagos, S.: Radiative impact of mineral dust on monsoon precipitation variability over West Africa, Atmos. Chem. Phys., 11, 1879-1893, https://doi.org/10.5194/acp-11-1879-2011, 2011.

Zhao, C., Chen, S., Leung, L. R., Qian, Y., Kok, J. F., Zaveri, R. A., and Huang, J.: Uncertainty in modeling dust mass balance and radiative forcing from size parameterization, Atmos. Chem. Phys., 13, 10733-10753, https://doi.org/10.5194/acp-13-10733-2013, 2013.

Zhao, C., Leung, L. R., Park, S.-H., Hagos, S., Lu, J., Sakaguchi, K., Yoon, J.-H., Harrop, B. E., Skamarock, W., and Duda, M. G.: Exploring the impacts of physics and resolution on aqua-planet simulations from a nonhydrostatic global variable-resolution modeling framework, J. Adv. Model. Earth Syst., 8, 1751-1768, https://doi.org/10.1002/2016MS000727, 2016.

Zhao, C., Xu, M., Wang, Y., Zhang, M., Guo, J., Hu, Z., Leung, L. R., Duda, M., and Skamarock, W.: Modeling extreme precipitation over East China with a global variable-resolution modeling framework (MPASv5.2): Impacts of resolution and physics, Geosci. Model Dev., 12, 2707-2726, https://doi.org/10.5194/gmd-12-2707-2019, 2019.

https://doi.org/10.5194/egusphere-2026-3149
Preprint. Discussion started: 25 June 2026

1138 **Table 1.** Dust size-bin boundaries and emitted volume fractions.

Bin	D_L (μm)	D_U (μm)	D_G (μm)	Volume fraction
1	0.0390625	0.078125	0.05524	7.70×10^{-7}
2	0.078125	0.15625	0.11048	1.50×10^{-5}
3	0.15625	0.3125	0.22097	1.90×10^{-4}
4	0.3125	0.625	0.44194	1.80×10^{-3}
5	0.625	1.25	0.88388	1.19×10^{-2}
6	1.25	2.5	1.76776	5.74×10^{-2}
7	2.5	5	3.53553	2.02×10^{-1}
8	5	10	7.07106	4.56×10^{-1}
9	10	20	14.1421	2.70×10^{-1}
10	20	40	28.2843	2.94×10^{-4}

1139

https://doi.org/10.5194/egusphere-2026-3149
Preprint. Discussion started: 25 June 2026

Table 2. Regional evaluation of simulated daily mean 10-m wind speed against collocated NOAA surface-station observations during 13–16 March 2021 for three mesh configurations (U50 km, V16 km, and V4 km). The statistics include the temporal correlation coefficient (*r*) and normalized mean bias (NMB, %). Regional values of *r* are obtained by averaging station-based temporal correlations within each region.

Regions*	U50 km		V16 km		V4 km	
	r	NMB (%)	*r*	NMB (%)	*r*	NMB (%)
TKD	0.23	+8.14	0.56	+2.67	0.81	+2.81
MGD	0.15	−53.37	0.61	−14.43	0.87	−11.46
HC–WIM	0.05	−61.73	0.87	−13.92	0.92	−10.17
LP	0.21	+26.71	0.73	+14.93	0.83	+12.83
NCP	0.18	+35.52	0.78	+8.02	0.84	+7.93
YRD	0.34	+29.51	0.71	+11.53	0.82	+9.56

* The locations and spatial extents of the analyzed regions are shown in **Fig. 1**.

https://doi.org/10.5194/egusphere-2026-3149
Preprint. Discussion started: 25 June 2026

Table 3. Total dust emissions over different regions during 13–17 March 2021.

Regions*	U50 km (Tg)	V16 km (Tg)	V4 km (Tg)	V16 km Relative Change (%)**	V4 km Relative Change (%)**
EA	322.825	436.603	500.301	35.24%	54.98%
TKD	72.401	102.021	105.412	40.91%	45.59%
MGD	140.841	194.115	232.920	37.83%	65.38%
HC–WIM	33.760	44.497	52.172	31.80%	54.54%
LP	1.625	1.911	2.642	17.60%	62.58%

* EA denotes East Asia (15–55°N, 70–140°E). The locations and spatial extents of the other analyzed regions are shown in **Fig. 1**. ** Relative change (%) is calculated relative to the U50 km simulation.

https://doi.org/10.5194/egusphere-2026-3149
Preprint. Discussion started: 25 June 2026

Table 4. Regional dust mass loading during 13–17 March 2021 for different mesh configurations.

Region	U50 km (Tg)	V16 km (Tg)	V4 km (Tg)	V16 km Relative Change (%)*	V4 km Relative Change (%)*
EA	75.094	85.394	92.744	13.72%	23.50%
TKD	10.391	12.914	13.869	24.28%	33.47%
MGD	13.893	16.766	19.751	20.68%	42.17%
HC–WIM	8.556	9.724	10.485	13.65%	22.55%
LP	2.703	2.909	2.563	7.62%	−5.18%
NCP	3.897	5.592	6.378	43.49%	63.66%
YRD	0.364	0.392	0.253	7.69%	−30.49%

* Relative change (%) is calculated relative to the U50 km simulation.

https://doi.org/10.5194/egusphere-2026-3149
Preprint. Discussion started: 25 June 2026

Table 5. Regional mean dust wet scavenging rate and total dust wet scavenging during 13–17 March 2021 in the U50 km and V4 km simulations.

Region	U50 km dust wet scavenging rate (mg m^{-2} day^{-1})	V4 km dust wet scavenging rate (mg m^{-2} day^{-1})	U50 km total dust wet scavenging (Tg)	V4 km total dust wet scavenging (Tg)
TKD	158.554	77.663	0.732	0.358
MGD	3.545	1.480	0.014	0.006
HC–WIM	74.261	15.966	0.226	0.048
LP	2.212	0.033	0.004	0.001
NCP	6.733	1.109	0.013	0.002
YRD	11.117	25.041	0.014	0.033

https://doi.org/10.5194/egusphere-2026-3149
Preprint. Discussion started: 25 June 2026

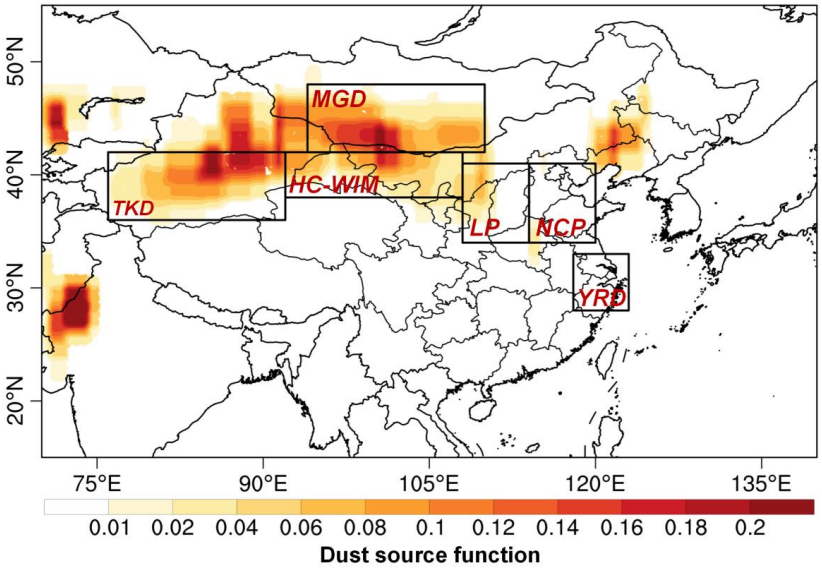

Fig. 1. Spatial distribution of the dust source function for the dust emission scheme in the model, and the major source and downwind regions analyzed in this study.

https://doi.org/10.5194/egusphere-2026-3149
Preprint. Discussion started: 25 June 2026

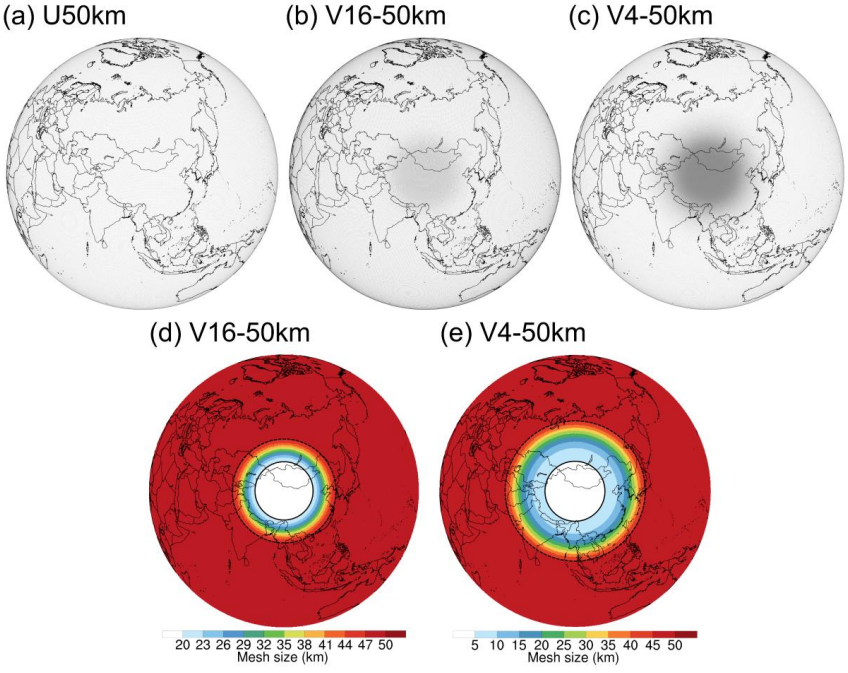

Fig. 2. (a) Global quasi-uniform mesh of 50 km (U50 km); (b, c) Global variable-resolution meshes of 16–50 km (V16 km) and 4–50 km (V4 km), refined over the major dust source regions in East Asia; (d, e) Spatial distributions of mesh spacing (cell size) for V16 km and V4 km. The black solid circles denote the refinement region, and the black dashed circles indicate the outermost boundary of the refinement transition zone.

https://doi.org/10.5194/egusphere-2026-3149
Preprint. Discussion started: 25 June 2026

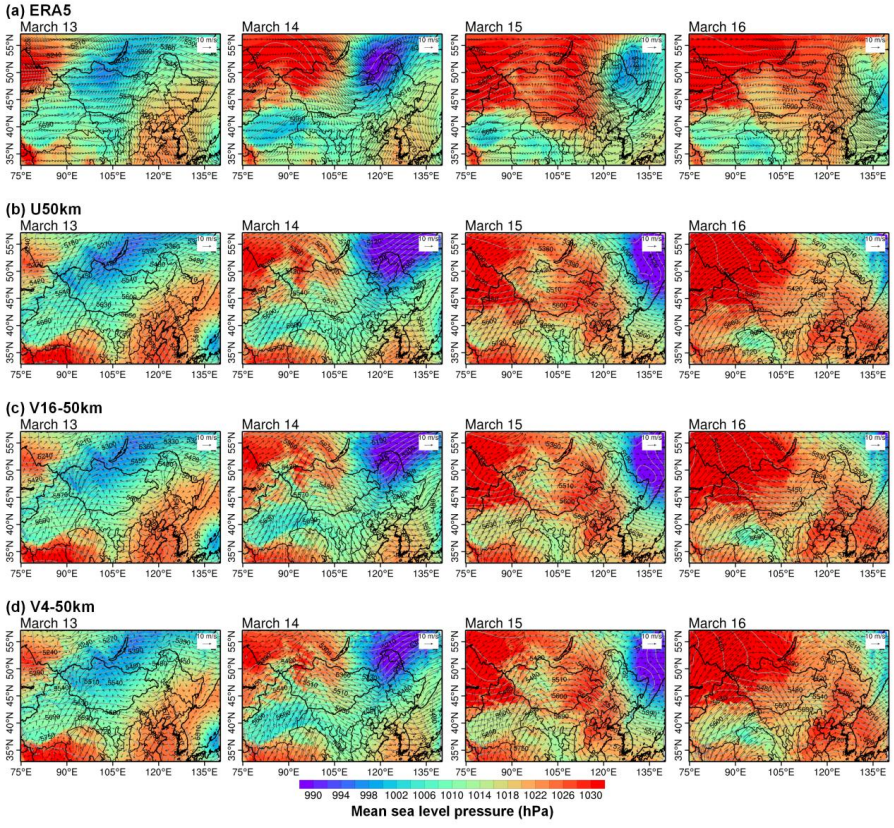

Fig. 3. Daily mean sea level pressure (shading, hPa), 500 hPa geopotential height (contours, gpm), and 850 hPa wind vectors for ERA5 and iAMAS simulations (U50 km, V16 km, and V4 km) during 13–16 March 2021.

https://doi.org/10.5194/egusphere-2026-3149
Preprint. Discussion started: 25 June 2026

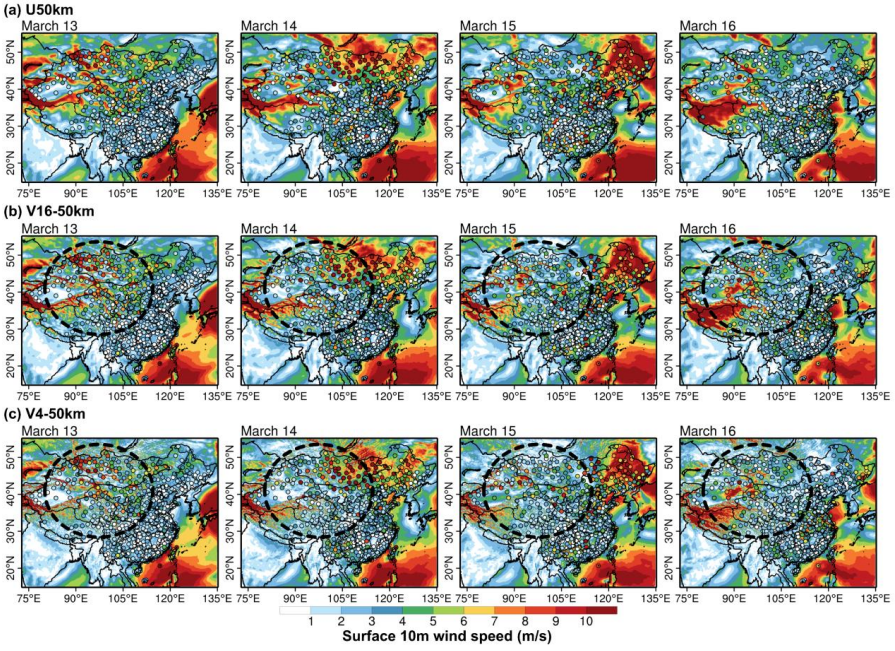

Fig. 4. Spatial distribution of daily mean 10-m wind speed (shading, m s^{-1}) from the iAMAS simulations (U50 km, V16 km, and V4 km), with collocated NOAA surface-station observations overlaid as colored markers, during 13–16 March 2021. The dashed outline denotes the refinement region.

https://doi.org/10.5194/egusphere-2026-3149
Preprint. Discussion started: 25 June 2026

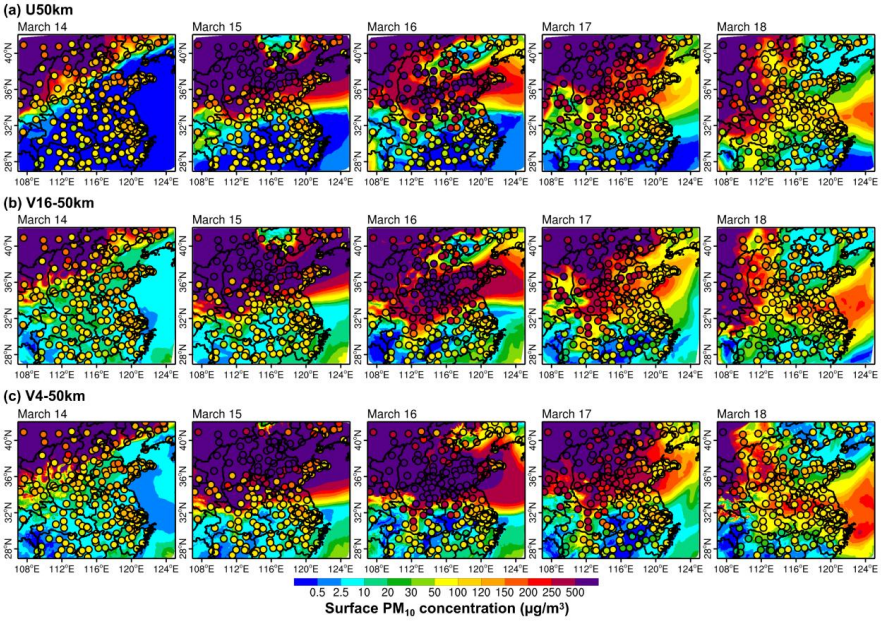

Fig. 5. Spatial distribution of daily mean surface PM_{10} concentrations over eastern China from the iAMAS simulations during 14–18 March 2021. Shading denotes simulated PM_{10} concentrations from the U50 km, V16 km, and V4 km configurations, and colored markers denote CNEMC observations at 192 collocated monitoring stations.

https://doi.org/10.5194/egusphere-2026-3149
Preprint. Discussion started: 25 June 2026

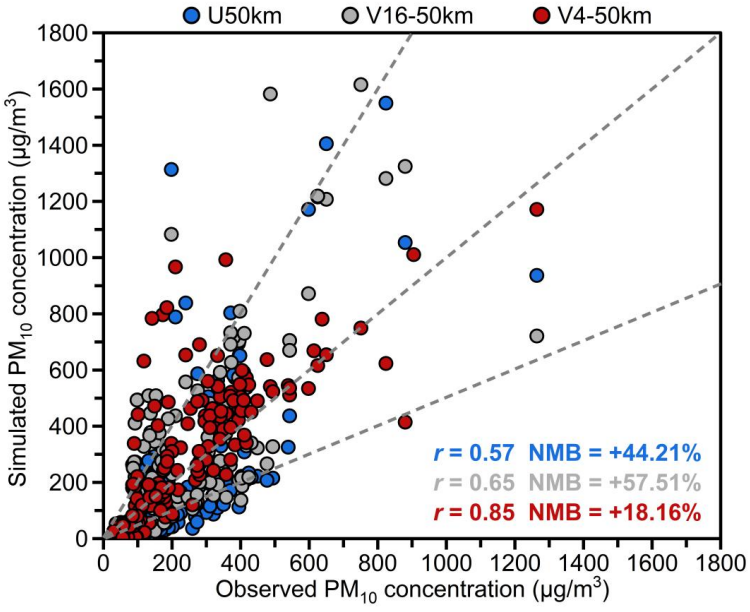

Fig. 6. Scatterplot of simulated versus observed period-mean surface PM_{10} concentrations over 14–18 March 2021 for different mesh configurations. Each marker corresponds to one of the 192 collocated CNEMC monitoring stations shown in **Fig. 5.** The correlation coefficient (r) and normalized mean bias (NMB, %) are shown for each experiment.

https://doi.org/10.5194/egusphere-2026-3149
Preprint. Discussion started: 25 June 2026

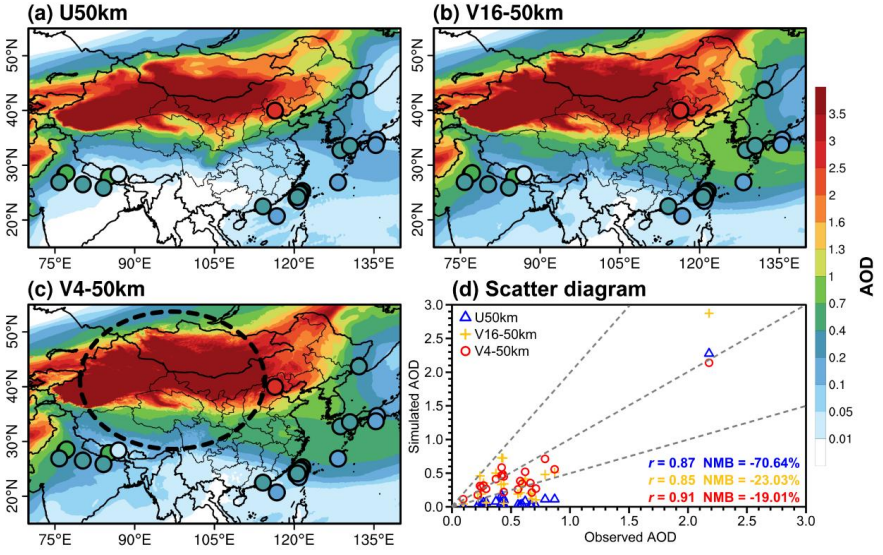

Fig. 7. (a–c) Spatial distribution of mean AOD at 500 nm averaged over 13–18 March 2021 from the iAMAS simulations using the U50 km, V16 km, and V4 km mesh configurations, with collocated AERONET observations overlaid as markers. (d) Scatterplot of simulated versus observed period-mean AOD at 500 nm at the collocated AERONET sites, with the correlation coefficient (r) and normalized mean bias (NMB) reported for each configuration. The dashed outline denotes the refinement region.

https://doi.org/10.5194/egusphere-2026-3149
Preprint. Discussion started: 25 June 2026

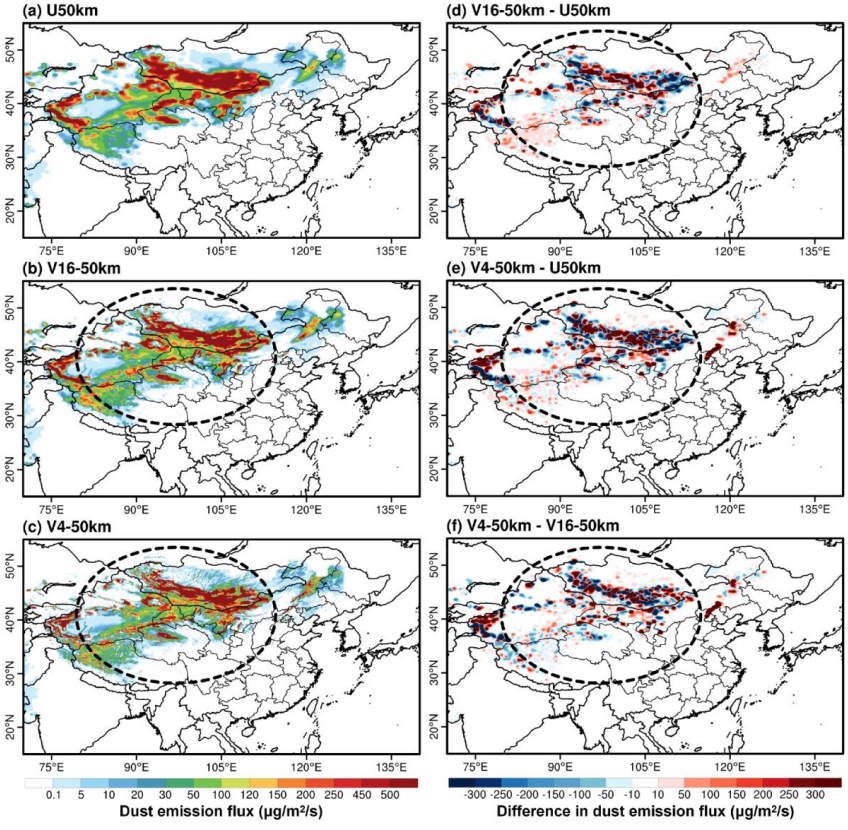

Fig. 8. (a–c) Spatial distribution of mean dust emission flux (μg m^{-2} s^{-1}) simulated with the U50 km, V16 km, and V4 km mesh configurations during 13–17 March 2021. (d) Differences in dust emission flux between V16 km and U50 km. (e) Differences between V4 km and U50 km. (f) Differences between V4 km and V16 km. The dashed outline denotes the refinement region.

https://doi.org/10.5194/egusphere-2026-3149
Preprint. Discussion started: 25 June 2026

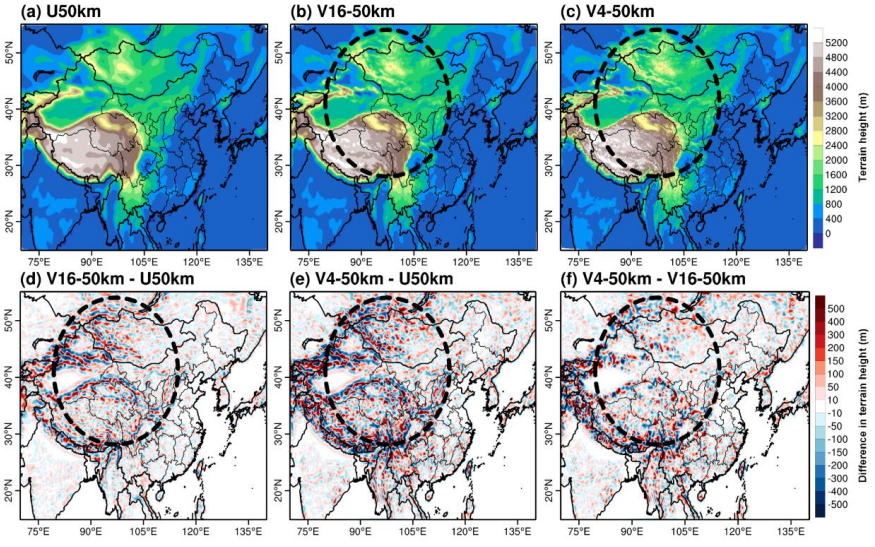

Fig. 9. (a–c) Spatial distribution of terrain height (m) for the U50 km, V16 km, and V4 km. (d) Differences in terrain height between V16 km and U50 km. (e) Differences between V4 km and U50 km. (f) Differences between V4 km and V16 km. The dashed outline denotes the refinement region.

https://doi.org/10.5194/egusphere-2026-3149
Preprint. Discussion started: 25 June 2026

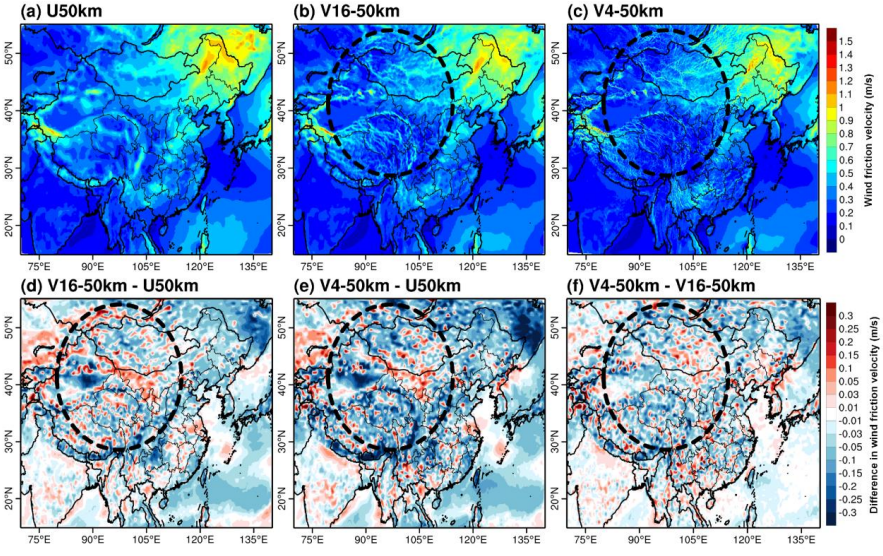

Fig. 10. (a–c) Spatial distribution of wind friction velocity (m s^{-1}) for the U50 km, V16 km, and V4 km during 13–17 March 2021. (d) Differences in wind friction velocity between V16 km and U50 km. (e) Differences between V4 km and U50 km. (f) Differences between V4 km and V16 km. The dashed outline denotes the refinement region.

https://doi.org/10.5194/egusphere-2026-3149
Preprint. Discussion started: 25 June 2026

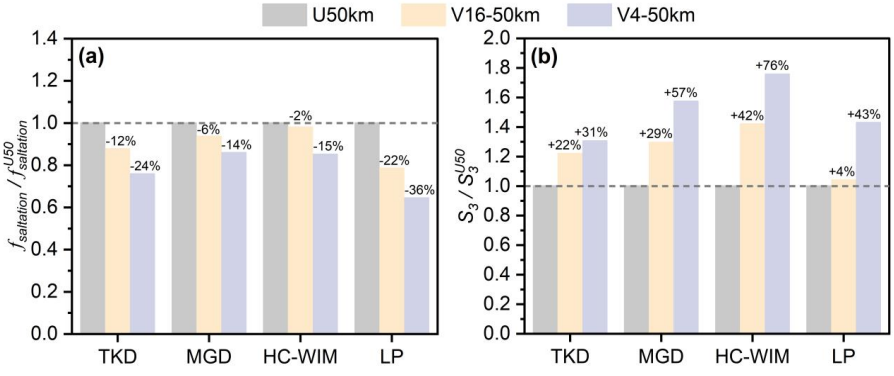

Fig. 11. Relative changes in saltation occurrence frequency ($f_{saltation}$) and the nonlinear amplification metric S_3 under different mesh configurations relative to the U50 km simulation.

https://doi.org/10.5194/egusphere-2026-3149
Preprint. Discussion started: 25 June 2026

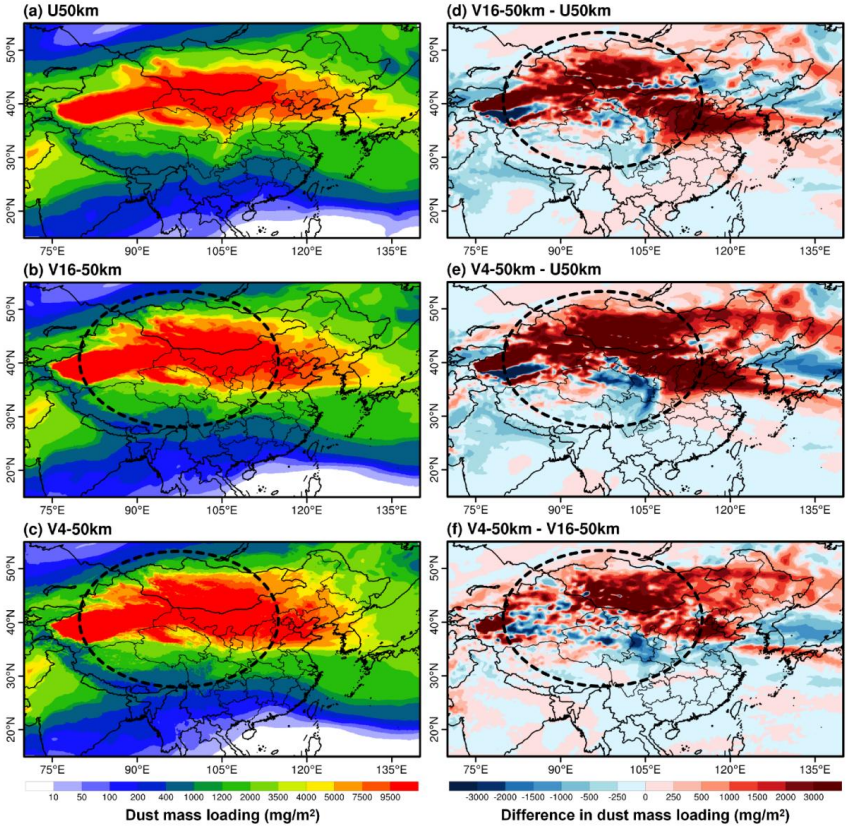

Fig. 12. (a–c) Spatial distribution of dust mass loading (mg m^{-2}) from the U50 km, V16 km, and V4 km simulations during 13–17 March 2021. (d) Differences in dust mass loading between V16 km and U50 km. (e) Differences between V4 km and U50 km. (f) Differences between V4 km and V16 km. The dashed outline denotes the refinement region.

https://doi.org/10.5194/egusphere-2026-3149
Preprint. Discussion started: 25 June 2026

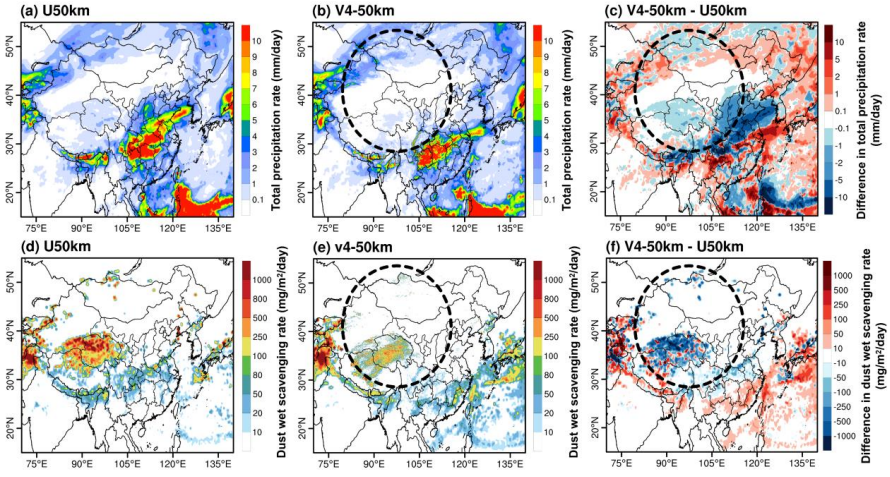

Fig. 13. (a–b) Spatial distributions of period-mean total precipitation rate (mm day^{-1}) from the U50 km and V4 km simulations during 13–17 March 2021. (c) Difference in period-mean total precipitation rate between V4 km and U50 km. (d–e) Spatial distributions of period-mean dust wet scavenging rate (mg m^{-2} day^{-1}) from the U50 km and V4 km simulations during 13–17 March 2021. (f) Difference in period-mean dust wet scavenging rate between V4 km and U50 km. The dashed outline denotes the refinement region.